Reconstruction of the phonon relaxation times using solutions of the Boltzmann transport equation

Mojtaba Forghani,[1] Nicolas G. Hadjiconstantinou,[1] and Jean-Philippe M. Péraud[2]

[1]*Department of Mechanical Engineering, Massachusetts Institute of Technology, Cambridge, Massachusetts 02139, USA*

[2]*Lawrence Berkeley National Laboratory, Berkeley, California 94720, USA*

We present a method for reconstructing the phonon relaxation time distribution $\tau_\omega = \tau(\omega)$ (including polarization) in a material from thermal spectroscopy data. The distinguishing feature of this approach is that it does not make use of the effective thermal conductivity concept and associated approximations. The reconstruction is posed as an optimization problem in which the relaxation times $\tau_\omega = \tau(\omega)$ are determined by minimizing the discrepancy between the experimental relaxation traces and solutions of the Boltzmann transport equation for the same problem. The latter may be analytical, in which case the procedure is very efficient, or numerical. The proposed method is illustrated using Monte Carlo solutions of thermal grating relaxation as synthetic experimental data. The reconstruction is shown to agree very well with the relaxation times used to generate the synthetic Monte Carlo data and remains robust in the presence of uncertainty (noise).

I. INTRODUCTION

By probing the thermal response at timescales and length scales on the order of the phonon relaxation times and free paths, respectively, thermal spectroscopy provides a potentially powerful means of extracting information about these intrinsic transport properties of real materials [1–6]. As a result, thermal spectroscopy has recently received a lot of attention for applications related to the development of thermoelectric materials [7,8].

The success of this technique relies on reliably extracting the information embedded in the material response, an inverse problem of considerable complexity that currently remains open. In order to use precise language, in this paper we focus on time-domain thermoreflectance. We believe that the methodology proposed in this paper can be straightforwardly extended to complementary approaches based on frequency-domain thermoreflectance [2–4].

Traditional approaches to time-domain thermoreflectance data analysis start by matching (in a least-squares-fit sense) the experimental response to numerical solutions of the heat conduction equation with the thermal conductivity treated as an adjustable, effective, quantity [8]. The free path distribution is subsequently extracted by assuming that the fitted effective thermal conductivity is given by the convolution of the differential free path distribution in the material with a suppression function that is assumed to be geometry dependent [5,9]. An approximate suppression function has been developed for the thermal grating geometry [5,10]; suppression functions for other, more complex, geometries have yet to be developed. Robust optimization frameworks for inverting the resulting integral equations have also been developed [7].

However, since, by design, the material response in the experiment is not in the traditional Fourier regime—defined by characteristic timescales and length scales being much longer than the phonon mean-free time and mean-free path, respectively—approaches based on fitting the material response using Fourier theory can only be accepted as approximate. This is highlighted in Sec. IV, where the case of the one-dimensional transient thermal grating (TTG), which ad-

mits an analytical solution, is analyzed in detail. This analysis shows that the requirement of long times is particularly difficult to satisfy even if corrections are applied for length-scale effects. In general, in situations where the requirements for Fourier behavior are not carefully met, the effective thermal conductivity obtained by such fits will depend on the fitting time window, the measurement location [11], and the experimental geometry, highlighting the fact that it is not a material property and casting doubt over the reliability of the inverse calculation.

To avoid these conceptual, but also practical, problems, in the present work we propose a methodology for reconstructing the relaxation time distribution in the material from thermal spectroscopy experimental results using an approach that at no time makes an assumption of an underlying Fourier behavior. In our work, the reconstruction problem is formulated as a nonconvex optimization problem whose goal is to minimize the difference between the experimental material response and the response as calculated by a Boltzmann transport equation (BTE)-based model of the experimental process. Here, we note the recent paper [12] in which reconstruction is based on a Fourier-space solution of a BTE model of the two-dimensional transient thermal grating experiment. Despite emphasizing the BTE more than in previous approaches, the work in Ref. [12], ultimately, still reverts to a Fourier-based formulation by fitting effective thermal diffusivities and introducing related approximations (e.g., late times compared to the mean phonon relaxation time).

A further distinguishing feature of our work is the use of deviational Monte Carlo (MC) simulation [13–16] as a method for solving the BTE, which expands the domain of applicability of the approach, since it does not rely on the simplicity of the experimental setup or the degree to which it is amenable to analytical treatment.

The remainder of the paper is organized as follows. In Sec. II, we formulate the reconstruction as an optimization problem requiring only solutions of the BTE and present the optimization framework used for the reconstruction. In Sec. III, we discuss the implementation of the proposed method in the

context of an archetypal experimental setup, namely that of a transient thermal grating [10,12,17]. In the same section, we validate our proposed method using synthetic data generated through MC simulation. In Sec. IV we provide a detailed theoretical analysis of the one-dimensional TTG problem as a means of highlighting the approximations associated with the effective thermal conductivity approach. In Sec. V we provide a summary of our work and suggestions for future improvement.

II. FORMULATION

A. Governing equations

Given the small temperature differences usually associated with thermal spectroscopy experiments, here we consider the linearized BTE

$$\frac{\partial e^d}{\partial t} + \mathbf{v}_\omega \cdot \boldsymbol{\nabla}_\mathbf{x} e^d = -\frac{e^d - (de^{eq}/dT)_{T_{eq}} \Delta \widetilde{T}}{\tau_\omega}, \qquad (1)$$

where $e^d = e^d(t,\mathbf{x},\omega,\boldsymbol{\Omega}) = e - e^{eq}_{T_{eq}} = \hbar\omega(f - f^{eq}_{T_{eq}})$ is the deviational energy distribution, ω is the phonon frequency, $\boldsymbol{\Omega}$ is the phonon traveling direction, $f = f(t,\mathbf{x},\omega,\boldsymbol{\Omega})$ is the occupation number of phonon modes, $\mathbf{v}_\omega = \mathbf{v}(\omega)$ is the phonon group velocity, $\tau_\omega = \tau(\omega)$ is the frequency-dependent relaxation time, and $\hbar$ is the reduced Planck constant. Here and in what follows, we use ω to denote the dependence on both frequency and polarization.

The above equation is linearized about the equilibrium temperature T_{eq}, to be understood here as the experimental reference temperature. In general, $\tau_\omega = \tau(\omega,T)$; however, as a result of the linearization, $\tau_\omega = \tau(\omega,T_{eq}) \equiv \tau(\omega)$; in other words, the solutions (and associated reconstruction) are valid for the experiment baseline temperature T_{eq}. Also, $(de^{eq}/dT)_{T_{eq}} = \hbar\omega(df^{eq}_T/dT)|_{T_{eq}}$ and f^{eq}_T is the Bose-Einstein distribution with temperature parameter T, given by

$$f^{eq}_T(\omega) = \frac{1}{\exp(\hbar\omega/k_B T) - 1}, \qquad (2)$$

where k_B is Boltzmann's constant. Finally, $\Delta\widetilde{T} = \Delta\widetilde{T}(t,\mathbf{x}) = \widetilde{T} - T_{eq}$ is referred to as the deviational pseudotemperature [$\widetilde{T}(t,\mathbf{x})$ is the pseudotemperature]. Note that the deviational pseudotemperature, which is different from the deviational temperature defined below, is defined by the energy conservation statement [15]

$$\int_{\boldsymbol{\Omega}} \int_\omega \left[\frac{C_\omega}{\tau_\omega} \Delta\widetilde{T} - \frac{e^d}{\tau_\omega} D_\omega \right] d\omega \, d\boldsymbol{\Omega} = 0, \qquad (3)$$

in which $D_\omega = D(\omega)$ is the density of states, $C_\omega = C(\omega; T_{eq}) = D_\omega (de^{eq}/dT)_{T_{eq}}$ is the frequency-dependent volumetric heat capacity, and $d\boldsymbol{\Omega} = \sin(\theta)d\theta d\phi$ represents the differential solid angle element such that θ and ϕ refer to the polar and azimuthal angles in the spherical coordinate system, respectively. The temperature $T(t,\mathbf{x})$ is computed from

$$\int_{\boldsymbol{\Omega}} \int_\omega [C_\omega \Delta T - e^d D_\omega] d\omega \, d\boldsymbol{\Omega} = 0, \qquad (4)$$

where $\Delta T(t,\mathbf{x}) = T - T_{eq}$ is the deviational temperature. The frequency-dependent free path is given by

$$\Lambda_\omega = v_\omega \tau_\omega, \qquad (5)$$

where $v_\omega = ||\mathbf{v}_\omega||$ is the group velocity magnitude.

B. Inverse problem formulation

Our goal is to obtain an accurate and reliable approximation to the function τ_ω from the experimental measurements, with the latter typically in the form of a temperature (relaxation) profile. Reconstruction of the free path distribution follows from relationship (5); in other words, the group velocities v_ω are assumed known, since they can be reliably calculated either experimentally [18–21] by means of Raman spectroscopy, x-ray scattering, etc., or theoretically [22–25] using methods such as density functional theory (DFT).

We propose the use of an optimization framework in which the experimental measurements provide targets that need to be reproduced by the BTE solution; in other words, τ_ω is determined as the function that optimizes (minimizes) the discrepancy between the experimental result and the BTE prediction for the same quantity. One important consideration is use of a suitable discrete representation for τ_ω. In our formulation any number of longitudinal/transverse acoustic/optical branches τ^S_ω may exist and are solved for explicitly, where the superscript S denotes the branch; the total scattering rate τ^{-1}_ω is obtained using Matthiessen's rule. In the examples following below we have taken

$$\tau^{-1}_\omega = \left(\tau^{LA}_\omega\right)^{-1} + \left(\tau^{TA_1}_\omega\right)^{-1} + \left(\tau^{TA_2}_\omega\right)^{-1}, \qquad (6)$$

where LA denotes the longitudinal acoustic branch, while TA_1 and TA_2 represent the two transverse acoustic branches. We have not considered optical phonons in this work because acoustic modes account for most of the heat conduction [26], but also because the proposed methodology can be straightforwardly extended to include them. Although the inclusion of additional unknowns is expected to have an effect on the complexity of the optimization calculation, as long as the number of additional unknowns is not large, this is manageable. Moreover, the weaker dependence of optical phonons on frequency may allow a simpler model introducing less unknowns than an additional acoustic branch. Also note that the contribution of optical phonons to transient transport is small and thus probably insufficient for the determination of an inverse problem with many unknowns.

In order to account for the most general situation where no *a priori* information is available on the functional form of the $\tau_\omega = \tau(\omega)$ relation, we have used a piecewise linear relation between $\log(\tau^S_\omega)$ and $\log(\omega)$. The intersections between the piecewise linear segments are smoothed via a third-order polynomial function [of $\log(\omega)$] that guarantees continuity of the relaxation time function and its first derivative (the continuity requirement may be easily removed, allowing jumps between different segments). Note that our parametrization is equivalent to a (piecewise) relationship of the form of $\tau_\omega = c_1 \omega^{c_2}$ for some real numbers c_1 and c_2, which is related

to relations commonly used in the literature [26,27]. Our approach, however, does not constrain the value of c_2 to any particular value or even an integer value. The actual functional form is given by

$$\log\left(\tau_\omega^S\right) = \sum_{j=0}^{M-1} \left\{ \frac{\log\left(\tau_{\omega_{j+1}}^S\right) - \log\left(\tau_{\omega_j}^S\right)}{\log\left(\omega_{j+1}^S\right) - \log\left(\omega_j^S\right)} \left[\log(\omega) - \log\left(\omega_j^S\right) \right] + \log\left(\tau_{\omega_j}^S\right) \right\} \mathbb{1}_{\omega \in [X_{2j}^S, X_{2j+1}^S]}$$

$$+ \sum_{j=1}^{M-1} \left\{ a_j^S [\log(\omega)]^3 + b_j^S [\log(\omega)]^2 + c_j^S \log(\omega) + d_j^S \right\} \mathbb{1}_{\omega \in (X_{2j-1}^S, X_{2j}^S)}, \tag{7}$$

where M determines the number of segments. We note that since the minimum and maximum frequencies for each branch (ω_0^S and ω_M^S) are known (input), there are $2M$ unknowns in the model for each branch $S \in \{LA, TA_1, TA_2\}$, consisting of $\omega_1^S, \ldots, \omega_{M-1}^S$, and $\log(\tau_{\omega_0}^S), \ldots, \log(\tau_{\omega_M}^S)$, leading to a total of $6M$ unknowns (see Sec. II C for implementation details; also note the input unknowns are denoted $\mathbf{p}^k$ in that section). In the above, $\mathbb{1}_{\omega \in \mathcal{S}}$ denotes the indicator function whose value is 1 if $\omega \in \mathcal{S}$, and 0 if $\omega \notin \mathcal{S}$. The closed intervals $[X_{2j}^S, X_{2j+1}^S]$ for $j = 0, \ldots, M-1$ and open intervals (X_{2j-1}^S, X_{2j}^S) for $j = 1, \ldots, M-1$ denote the frequency ranges over which the piecewise linear and smoothing polynomial functions are active, respectively; definitions for $X_i^S, i = 0, \ldots, 2M-1$ can be found in Appendix A.

Once all ω_j^S and $\log(\tau_{\omega_j}^S)$ are known, the coefficients a_j^S, b_j^S, c_j^S, d_j^S, and the intervals in which each linear segment or polynomial smoothing function is active inside can be computed. The relationships for calculating these parameters are provided in Appendix A.

In the interest of compactness, we will use the vectorial notations $\boldsymbol{\tau}^S = (\tau_{\omega_0}^S, \ldots, \tau_{\omega_M}^S)$ and $\boldsymbol{\omega}^S = (\omega_1^S, \ldots, \omega_{M-1}^S)$ to represent the unknown parameters. Moreover, we will use the symbol $\mathbf{U}$ to denote the set of all unknown vectors, namely, $\mathbf{U} = (\boldsymbol{\tau}^{LA}, \boldsymbol{\tau}^{TA_1}, \boldsymbol{\tau}^{TA_2}, \boldsymbol{\omega}^{LA}, \boldsymbol{\omega}^{TA_1}, \boldsymbol{\omega}^{TA_2})$.

The reconstruction proceeds by minimizing the objective function

$$\mathcal{L} = \min_{\mathbf{U}} \left[\frac{\sum_{t,\mathbf{x},L} |T_m(t,\mathbf{x};L) - T_{BTE}(t,\mathbf{x};L,\mathbf{U})|}{N} \right.$$
$$\left. + \alpha \left| 1 - \frac{1}{3\kappa} \int_\omega C_\omega \tau_\omega(\mathbf{U}) v_\omega^2 d\omega \right| \right], \tag{8}$$

where $T_m(t,\mathbf{x};L)$ denotes the experimentally measured temperature, T_{BTE} is the temperature computed from solution of the BTE, and N is the total number of (independent) measurements available. As indicated above, T_m is in general a function of space, time, but also the characteristic length scale of the thermal relaxation problem, L. As a result, the optimization process can be based on data for T_{BTE} and T_m at various time instances, spatial locations, and for different characteristic system parameters, with $\sum_{t,\mathbf{x},L} 1 = N$. We also point out that T_{BTE} may be obtained by any method that can provide accurate solutions of (1) as applied to the experimental setup; here, we consider both semianalytical solution (using Fourier transform techniques) and MC simulation.

The second term in (8) exploits the fact that the bulk value of the thermal conductivity, κ, is usually known, to enhance the importance of the low-frequency modes in the optimization. Although this term is optional, we have found that including this term with a weight of $0.01 < \alpha < 1$ improves the reconstruction quality considerably in the low-frequency regime, because the low density of states associated with those frequencies prevents them from influencing the optimization process if the objective function only includes a comparison between T_{BTE} and T_m [the first term in (8)].

C. Optimization algorithm

Determination of $\mathbf{U}$ which minimizes the objective function (8) is achieved using the Nelder-Mead (NM) algorithm [28], a simplex-based search method that is free from gradient computation. Although NM can neither be categorized as a local optimizer or a global optimizer, it performs significantly better than common local minimizers [which fail to converge to the correct solution in the presence of highly nonconvex objective functions such as (8)] [29], while it is significantly less costly than common global optimizers such as genetic algorithms [30] or simulated annealing algorithms [31].

In the NM algorithm, the optimization process proceeds as follows (adopted from Ref. [32]).

(i) Start with $n + 1$ initial points $\mathbf{p}^k$, $k = 0, \ldots, n$, in the n-dimensional space defined by the n unknown parameters (here $n = 6M$). A possible choice of initial simplex (the set of $n + 1$ initial points) is $\mathbf{p}^0$ and $\mathbf{p}^k = \mathbf{p}^0 + \delta_k \mathbf{e}_k$ for scalars δ_k, $k = 1, \ldots, n$; here $\mathbf{p}^0$ is an arbitrary point in the n-dimensional space of unknown parameters and $\mathbf{e}_k$ is the unit vector in the kth direction [33].

(ii) Order the points $\mathbf{p}^k$, $k = 0, \ldots, n$, in an ascending order based on their objective function values. Assign new superscripts such that $\mathcal{L}(\mathbf{p}^0) \leqslant \ldots \leqslant \mathcal{L}(\mathbf{p}^{n-1}) \leqslant \mathcal{L}(\mathbf{p}^n)$.

(iii) Calculate the centroid of the n points with lowest objective function values, $\mathbf{p}^{cn} = \frac{1}{n} \sum_{k=0}^{n-1} \mathbf{p}^k$.

(iv) Calculate the reflected point, $\mathbf{p}^r = \mathbf{p}^{cn} + \mu(\mathbf{p}^{cn} - \mathbf{p}^n)$, where $\mu > 0$.

(v) If $\mathcal{L}(\mathbf{p}^0) \leqslant \mathcal{L}(\mathbf{p}^r) < \mathcal{L}(\mathbf{p}^{n-1})$, replace $\mathbf{p}^n$ with $\mathbf{p}^r$ and start the next iteration; go to step (ii).

(vi) If $\mathcal{L}(\mathbf{p}^r) < \mathcal{L}(\mathbf{p}^0)$, compute $\mathbf{p}^e = \mathbf{p}^r + \gamma(\mathbf{p}^r - \mathbf{p}^{cn})$, the expanded point, where $\gamma > 0$.

    (a) If $\mathcal{L}(\mathbf{p}^e) < \mathcal{L}(\mathbf{p}^r)$, replace $\mathbf{p}^n$ with $\mathbf{p}^e$ and start the next iteration; go to step (ii).

    (b) If $\mathcal{L}(\mathbf{p}^e) \geqslant \mathcal{L}(\mathbf{p}^r)$, replace $\mathbf{p}^n$ with $\mathbf{p}^r$ and start the next iteration; go to step (ii).

(vii) If $\mathcal{L}(\mathbf{p}^r) \geqslant \mathcal{L}(\mathbf{p}^{n-1})$

    (a) If $\mathcal{L}(\mathbf{p}^r) < \mathcal{L}(\mathbf{p}^n)$, compute $\mathbf{p}^c = \mathbf{p}^{cn} + \rho(\mathbf{p}^r - \mathbf{p}^{cn})$, the contracted point, where $0 < \rho < 1$.
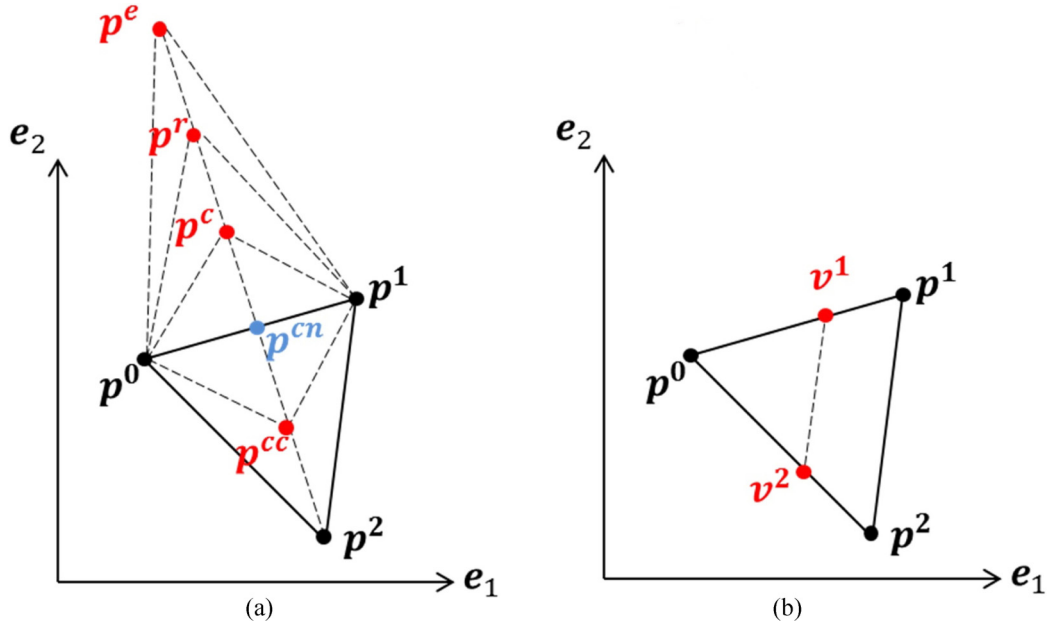
FIG. 1. An example of simplex update in the NM algorithm; the case of two unknowns (corresponding to $n = 2$) is shown. (a) Point $\mathbf{p}^2$ of the previous simplex (which consists of points $\mathbf{p}^0$, $\mathbf{p}^1$, and $\mathbf{p}^2$) is replaced with a new point from the set $\{\mathbf{p}^c, \mathbf{p}^{cc}, \mathbf{p}^r, \mathbf{p}^e\}$. The new simplex consists of $\mathbf{p}^0$, $\mathbf{p}^1$, and the replacement of $\mathbf{p}^2$. (b) If none of the candidate points in (a) have an objective function smaller than $\mathcal{L}(\mathbf{p}^2)$, then the simplex shrinks. The new simplex is $\mathbf{p}^0$, $\mathbf{v}^1$, and $\mathbf{v}^2$.

If $\mathcal{L}(\mathbf{p}^c) \leqslant \mathcal{L}(\mathbf{p}^r)$, replace $\mathbf{p}^n$ with $\mathbf{p}^c$ and start the next iteration; go to step (ii). Otherwise, go to step (viii).

(b) If $\mathcal{L}(\mathbf{p}^r) \geqslant \mathcal{L}(\mathbf{p}^n)$, compute $\mathbf{p}^{cc} = \mathbf{p}^{cn} + \rho(\mathbf{p}^n - \mathbf{p}^{cn})$, the new contracted point. If $\mathcal{L}(\mathbf{p}^{cc}) \leqslant \mathcal{L}(\mathbf{p}^n)$, replace $\mathbf{p}^n$ with $\mathbf{p}^{cc}$ and start the next iteration; go to step (ii). Otherwise, go to step (viii).

(viii) For $k = 1, \ldots, n$, compute $\mathbf{v}^k = \mathbf{p}^0 + \sigma(\mathbf{p}^k - \mathbf{p}^0)$ where $0 < \sigma < 1$, replace $\mathbf{p}^k$ with $\mathbf{v}^k$, and start the next iteration [go to step (ii)].

In words, in each iteration, the objective is to eliminate the worst point (with the largest value of objective function) among the current $n + 1$ points of the simplex via reflection [step (v) or (vi)b], expansion [step (vi)a], contraction [step (vii)] or shrinkage [step (viii)]. Figure 1 illustrates this algorithm for the case $n = 2$. In the present work, the parameters μ, γ, and ρ are taken to be 1, 1, and 0.5, respectively, as proposed in Refs. [28,32,34]. We have also chosen the shrinkage coefficient to be $\sigma = 0.9$ as recommended in Ref. [34] for robustness in the presence of noise.

The most expensive step in this process is the calculation of the objective function (8) which requires evaluation of T_{BTE}. The NM algorithm typically requires one or two evaluations of (8) at each iteration, except when a shrinkage step takes place where $6M + 2$ evaluations of (8) are required. Single function evaluation occurs as a result of successful initial reflection corresponding to step (v) of the algorithm. Two evaluations of the objective function result from either expansion at step (vi)a, reflection at step (vi)b, outside contraction at step (vii)a or inside contraction at step (vii)b. The simplex typically starts to shrink near the convergence point where the algorithm cannot find any new direction that yields lower values of the objective function, leading it to search for

such point inside the previous simplex by shrinking it toward its best vertex [34].

III. APPLICATION EXAMPLE AND VALIDATION

In this section, we consider the one-dimensional TTG experiment as an example for illustrating and validating the methodology presented in Sec. II. The mathematical model of the TTG experiment will be briefly discussed in Sec. III A. Using this mathematical formulation, we generate synthetic experimental data; this process is described in Sec. III B. We then use these synthetic data to reconstruct τ_ω for the material model used in the MC simulations; the details of the reconstruction process are discussed in Sec. III C. We consider reconstruction both via semianalytical solution of the BTE and MC simulation; the advantages of each approach are discussed and contrasted. In Sec. III D, we compare the reconstructed relaxation times and free path distribution with those of the original data used in the MC simulations for generating the synthetic data.

A. TTG experiment

The TTG experiment has been widely used to study transient thermal transport. In this experiment, a sinusoidal profile with unit amplitude is generated by crossing two short pump pulses [35]. By assuming one-dimensional heat transport along the x direction, the BTE from Eq. (1) can be written in the form

$$\frac{\partial e^d}{\partial t} + v_\omega \cos(\theta) \frac{\partial e^d}{\partial x} = -\frac{e^d - (de^{eq}/dT)_{T_{eq}} \Delta \widetilde{T}}{\tau_\omega}$$
$$+ (de^{eq}/dT)_{T_{eq}} \delta(t) e^{2\pi i x/L}, \quad (9)$$

in which the last term is due to the sinusoidal initial temperature profile. Here, L is the grating wavelength (see discussion in Sec. II B), and i is the imaginary unit. This equation is sufficiently tractable to allow analytical solutions in Fourier/reciprocal space [10,17]. We follow a similar procedure (see Appendix B) to obtain a Fourier space solution for T_{BTE}; the final result is

$$\Delta T_\zeta = \frac{e^{2\pi i x/L}}{C}\left[\int_\omega S_\omega \tau_\omega^2 d\omega + \frac{\left(\int_\omega S_\omega \tau_\omega d\omega\right)^2}{\int_\omega \left[C_\omega \tau_\omega^{-1} - S_\omega\right]d\omega}\right], \quad (10)$$

where $C = \int_\omega C_\omega d\omega$ is the volumetric heat capacity and $\Delta T_\zeta = \Delta T(\zeta, x)$ denotes the Fourier transform of $\Delta T(t, x)$ with respect to the time variable. Also, $S_\omega = S(\omega, \zeta)$ is given by

$$S_\omega = \frac{iC_\omega L}{4\pi v_\omega \tau_\omega^2}\ln\left(\frac{\tau_\omega \zeta - v_\omega \tau_\omega 2\pi L^{-1} - i}{\tau_\omega \zeta + v_\omega \tau_\omega 2\pi L^{-1} - i}\right). \quad (11)$$

We note here that the temperature profile required for evaluating (8) is given by $T_{BTE}(t, x) = \Delta T(t, x) + T_{eq}$.

B. Generation of synthetic experimental data

Instead of using experimental data (for T_m) to validate the proposed methodology, we use synthetic data generated from MC simulation of (9). This approach enables considerably more precise validation because it sidesteps issues of experimental error, which is hard to quantify, but also of modeling error [how accurately does (9) model the TTG experiment?], which is even harder to quantify. In other words, reconstruction from T_m measurements obtained from MC simulations should be able to reproduce the function τ_ω used to generate the synthetic data exactly, making any discrepancies directly attributable to numerical/methodological error.

In the interest of simplicity, the material was assumed to be silicon. However, in order to fully explore the ability of the reconstruction process to capture arbitrary functional relations $\tau_\omega = \tau(\omega)$, we consider both a simple analytical model and an *ab initio* model of this material. The simple model considered here is described in Refs. [13,36] (thermal conductivity $\kappa = 143.8$ Wm^{-1} K^{-1}) and will be referred to as the Holland model. The second model considered (thermal conductivity $\kappa = 139.7$ Wm^{-1} K^{-1}) is described in Ref. [17] and will be referred to as the *ab initio* model throughout this paper.

Mirroring the experimental procedure as closely as possible, we obtain transient temperature relaxation data [solutions of (9)] at one spatial location for a number of characteristic (grating) lengths, namely $T_m(0 \leqslant t \leqslant t_L; L)$ [$=T_m(0 \leqslant t \leqslant t_L, x = 0; L)$ for example]. These solutions were obtained using the adjoint Monte Carlo method recently proposed [16] that is particularly efficient if solutions at particular spatial locations are of interest. The MC simulations used a sufficiently high number of particles ($\mathcal{N}_m = 10^9$) to ensure that the synthetic data was essentially noise free. As discussed in Sec. III D, we have also produced noisy synthetic data using significantly fewer particles in order to investigate the robustness of the optimization method to noise. Relaxation data was recorded in the time period $0 \leqslant t \leqslant t_L$, where $t_L = \min(t_{L,1\%}, 5$ ns); here, $t_{L,1\%}$ denotes the time taken for

the response to decay to 1% of its original amplitude for each L. During this time period, 100 discrete T_m measurements were obtained. Eight different wavelengths were simulated, namely, $L = 10$ nm, 50 nm, 100 nm, 500 nm, 1 μm, 5 μm, 10 μm, and 50 μm. As a result, 800 total T_m measurements were available for reconstruction ($N = 800$).

C. Reconstruction

Reconstruction proceeds by comparing solutions of the 1D TTG experiment, Eq. (9), in the form of $T_{BTE}(0 \leqslant t \leqslant t_L; L, \mathbf{U})$ to the counterpart N measurements of T_m as a means of finding the optimum unknown vectors. Here, solutions of (9) were obtained using inverse fast Fourier transform (IFFT) of (10) as explained in Ref. [37], or by using adjoint MC simulations [16]. Although MC simulations are more expensive, they are investigated here because they make the proposed method significantly more general, since they are not limited to problems which lend themselves to analytical or semianalytical solutions.

As discussed before, phonon group velocities were assumed known, while τ_ω was described by the model given in (7) with $M = 3$ (a piecewise linear function with three segments). As shown in Sec. III D, this approximation level gives very good results.

To generate the initial starting points ($6M + 1$ vertices of the simplex), we have used $\delta_k = 0.1 p_k^0$ as recommended in Ref. [33], where p_k^0 represents the kth component of vector $\mathbf{p}^0$ as discussed in the first step of the NM algorithm in Sec. II C. Larger values of δ_k (we have tested $\delta_k = 10 p_k^0$) may lead to large steps during the initial iterations of the optimization, which consequently can move the simplex toward a wrong local minimum; on the other hand, very small values of δ_k (we have tested $\delta_k = 0.001 p_k^0$) lead to smaller steps throughout the optimization process, which require a (significantly) larger number of iterations in order to guarantee that the parameter space is adequately sampled. We have obtained similar performances to $\delta_k = 0.1 p_k^0$ using $\delta_k = 0.05 p_k^0$ and $\delta_k = 0.025 p_k^0$.

We perform the optimization in four stages. In the first stage, we solve for one segment ($M = 1$), which is the same for all branches, leading to only two unknown parameters. Due to the small number of unknowns, this step is very cheap but very valuable since it results in a significant reduction in the value of objective function in only 10–20 iterations. In the second stage, LA and TA modes are still assumed to be the same but the intended number of segments is used, increasing the number of unknowns to $2M$ (six in the present case). The initial condition for this stage is taken to be the same as the optimized value of the previous stage (or a slightly perturbed version). In the third stage, we repeat the optimization process, now for $4M$ unknowns (the two TA branches are assumed to be the same, $\tau_\omega^{TA_1} = \tau_\omega^{TA_2}$), starting from the optimized parameters of the second stage. Finally, we perform the optimization for all $6M$ unknowns starting from the optimized parameters of the previous stage (repeated for each of the three branches independently). This procedure is more robust than direct optimization for $6M$ unknowns, which depending on the initial condition may be trapped in a
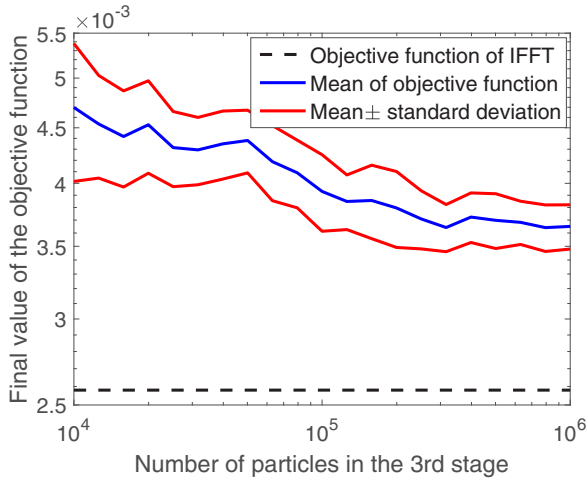
FIG. 2. Dependence of the final value of $\mathcal{L}$ at the third stage on $\mathcal{N}_{BTE}$. Increasing the number of particles decreases the mean and variance of $\mathcal{L}$.

local minimum of (8) characterized by significantly different relaxation times for the LA and TA branches.

To reduce the probability of the reconstruction being trapped in a local minimum, in our approach, the first and second stages were repeated starting from five distinct initial conditions. The result at each stage with the lowest value of $\mathcal{L}$ was used as the initial condition for the next stage. Although this consideration may not be necessary, it is expected to improve the quality of the optimization process (by providing a smaller final value of $\mathcal{L}$) due to the nonconvexity of the objective function.

Although the number of iterations varies depending on the initial condition, we have observed that for the value of M used in our work (corresponding to $6M = 18$ unknowns), the third and fourth stages require on the order of 150–200 iterations for convergence (each). When using analytical or semianalytical (IFFT) solutions for T_{BTE}, the computational cost associated with each evaluation is very small and thus

cost is not a consideration. Using MC simulation to obtain solutions for T_{BTE} is more costly and is discussed below.

1. Reconstruction using MC simulations

To reduce cost, MC simulations during the first two stages of the optimization process used $\mathcal{N}_{BTE} = 10^4$ particles for calculation of T_{BTE}. During the third and fourth stages of the process, the number of particles is increased to $\mathcal{N}_{BTE} = 10^6$.

Figure 2 investigates the sensitivity of the final value of the objective function $\mathcal{L}$ in the third stage as a function of the number of particles used (in this stage of the optimization) for the *ab initio* material model. Specifically, the figure compares the mean and variance of the objective function compared to the third-stage final value obtained from IFFT of (10) (which is free from noise and independent of number of particles). The MC result appears to converge (asymptotically) to the deterministic result with increasing number of computational particles, $\mathcal{N}_{BTE}$. Although this convergence appears to be slow, it is encouraging that the additional error (compared to deterministic reconstruction) is small and thus the shallow slope of the convergence implies that the reconstruction is quite robust to noise in the range $10^4 \leqslant \mathcal{N}_{BTE} \leqslant 10^6$.

Since the computational time for each adjoint MC simulation is proportional to $\mathcal{N}_{BTE}$ [16], given our choices for $\mathcal{N}_{BTE}$ ($\mathcal{N}_{BTE} = 10^4$ for stages 1 and 2 and $\mathcal{N}_{BTE} = 10^6$ for stages 3 and 4), the cost of the first two stages of the optimization is negligible compared to the cost of the last two stages. Here we note that no attempt has been made to optimize this process; it is therefore possible that considerably more computational benefits may be possible if a more structured approach is used [38] that takes into account information such as that contained in Fig. 2. We also note that given the small cost of the first two optimization stages, repeating them a number of times starting from different initial conditions does not increase the cost of the reconstruction process significantly.

For an average of 150–200 iterations, the cost of each of the third or fourth stages corresponds to 300–600 MC simulations, considering that on average 2–3 evaluations of (8)
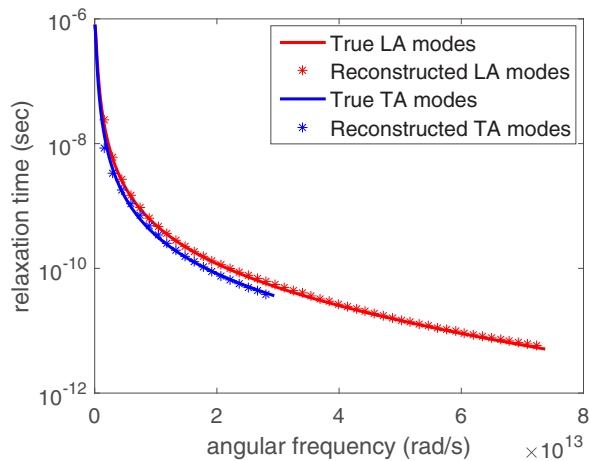
(a) relaxation times
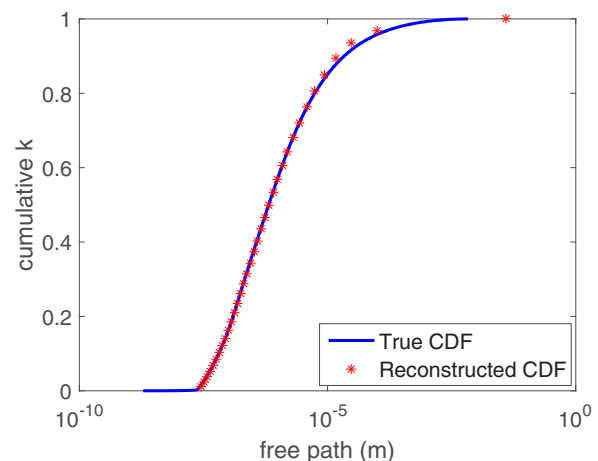
(b) free path distribution

FIG. 3. Comparison between true and reconstructed relaxation times and free path distribution using IFFT of the semianalytical result (10) for the Holland material model.

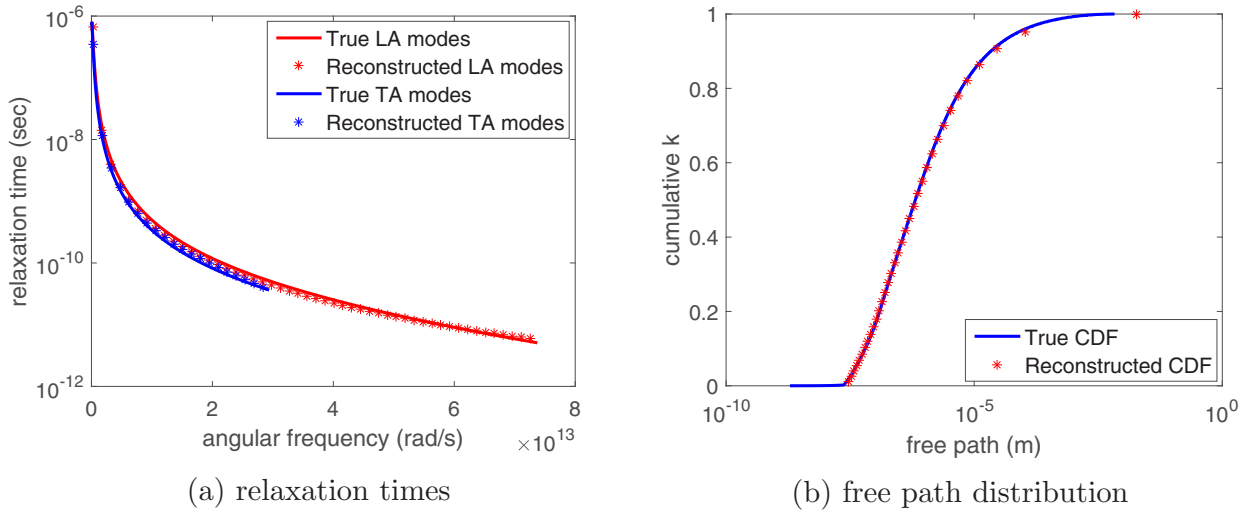(a) relaxation times

(b) free path distribution

FIG. 4. Comparison between true and reconstructed relaxation times and free path distribution using T_{BTE} obtained from adjoint MC simulation using the Holland material model.

at each iteration are required. This number of iterations can be performed efficiently using the adjoint method proposed recently in Ref. [16]. Note that a significant fraction of the computational effort is spent on iterations close to the final solution, which is primarily due to the high computational cost of the shrinkage step near convergence as was discussed previously in Sec. II C (compare $6M + 2 = 20$ function evaluations associated with the shrinkage step, with one or two function evaluations associated with reflection, expansion or contraction). In contrast to the present case where validation required very small error tolerances, in actual practice, tolerances will be set by experimental considerations and are expected to be larger, reducing the number of expensive shrinkage processes and making the cost of reconstruction from experimental data smaller.

D. Validation

In this section, we discuss reconstruction results with particular emphasis on their ability to reproduce the original

material properties [$\tau_\omega = \tau(\omega)$] used to generate the synthetic measurements T_m, referred to as true. Although our scheme returns τ_ω as output, as is typical in the literature, we also provide comparison between the true and reconstructed cumulative distribution function (CDF) of free paths referred to as "cumulative κ" and defined as $F(\Lambda) = \frac{1}{3\kappa} \int_{\omega^*(\Lambda)} C_\omega v_\omega^2 \tau_\omega d\omega$, where $\omega^*(\Lambda)$ is the set of modes such that $\omega^*(\Lambda) = \{\omega | \Lambda_\omega \leqslant \Lambda\}$.

1. Holland model

In this section, we present results for the Holland material model. For this model, we assumed that the two TA branches are the same and as a result, the optimization process consists of three stages with a total of $4M$ unknowns.

Figure 3 shows a comparison between the true material parameters and the reconstructed ones using the semianalytical solution (10) for T_{BTE}. The agreement is excellent.

Figure 4 shows a similar comparison for the case where MC simulations were used for obtaining T_{BTE}. We observe that the

(a) temperature profile for $L = 10\ nm$
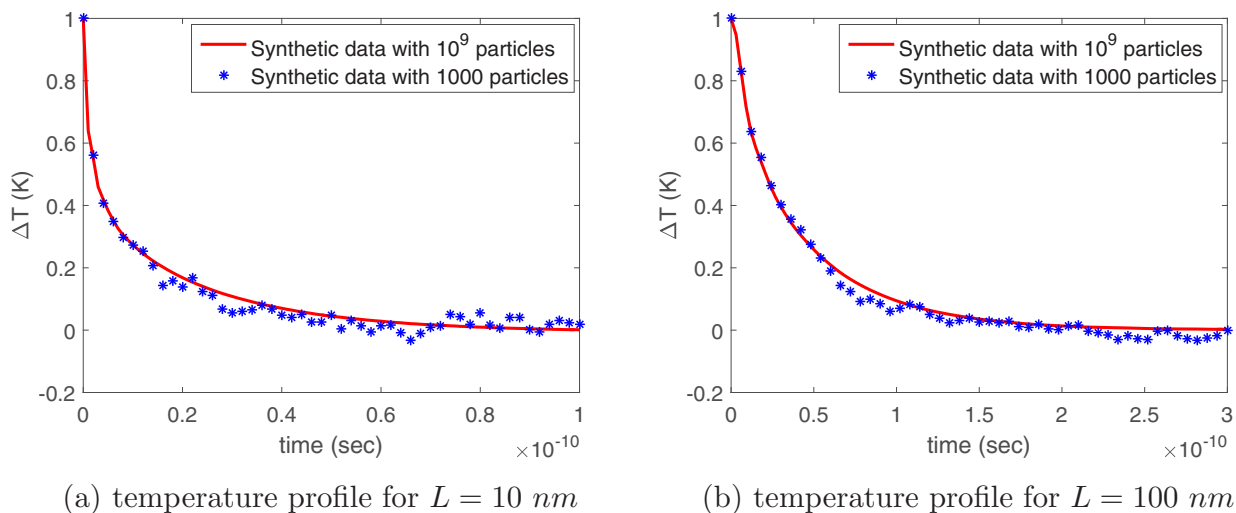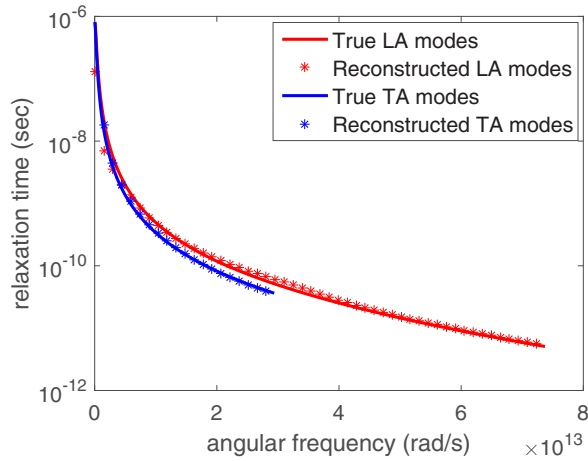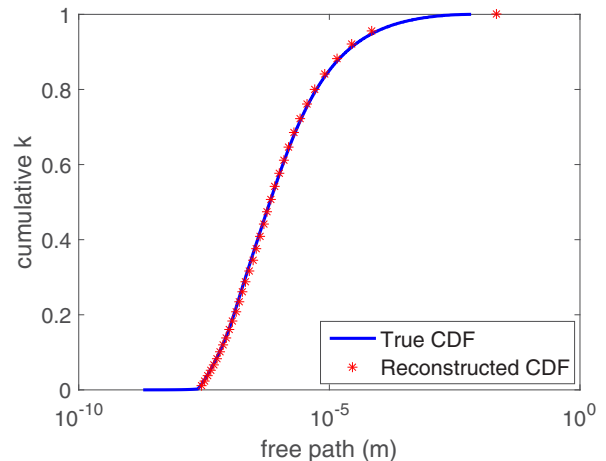

(b) temperature profile for $L = 100\ nm$

FIG. 5. Comparison of the synthetic temperature profile obtained by MC simulations using $\mathcal{N}_m = 10^9$ and $\mathcal{N}_m = 10^3$ computational particles based on the Holland material model. Two different grating wavelengths are shown.

(a) relaxation times

(b) free path distribution

FIG. 6. Comparison between true and reconstructed relaxation times and free path distribution using IFFT of (10) from noisy synthetic data for the Holland material model.

error in reconstructed relaxation times is more significant when using MC simulations. We attribute this primarily to the noise associated with MC simulation and its interaction with the NM algorithm.

The synthetic data used to obtain the results in Figs. 3 and 4 were generated by MC simulations using $\mathcal{N}_m = 10^9$ computational particles. This high number of computational particles leads to a very small variance, corresponding to a very accurate experimental measurement. In order to evaluate the performance of the reconstruction method in the presence of noise in the experimental measurement, we have also performed reconstruction calculations with noisy synthetic data. For that purpose, we have used only $\mathcal{N}_m = 10^3$ computational particles in the MC simulations that generated the synthetic data, leading to a standard deviation of 0.02 K. This number of particles makes the uncertainty in T_m significantly larger than the noise in common experimental data (e.g., compare the noisy temperature profile of Fig. 5 with

Fig. 2(c) of Ref. [8]). Figure 5 shows a comparison between the synthetic data obtained with $\mathcal{N}_m = 10^9$ and $\mathcal{N}_m = 10^3$ particles.
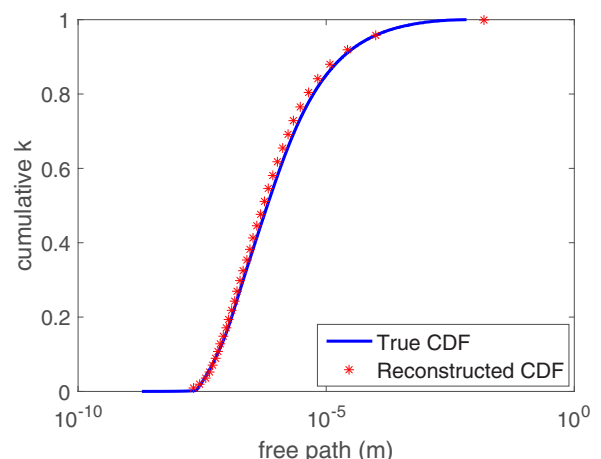
The reconstructed relaxation times and free path distribution corresponding to the noisy synthetic data ($\mathcal{N}_m = 10^3$) using semianalytical and MC solutions with the Holland material model are provided in Figs. 6 and 7, respectively. In both figures we observe that even in the presence of the considerable noise in the measurement, the algorithm is able to infer the relaxation times and the free path distribution with reasonable accuracy.

2. Ab initio model

In this section, we repeat the validation process, namely using IFFT of (10) and adjoint MC simulation in the presence and absence of noise in the synthetic data, for the *ab initio* material model. The reconstructed material properties in the absence of noise ($\mathcal{N}_m = 10^9$) are provided in Figs. 8 and 9.
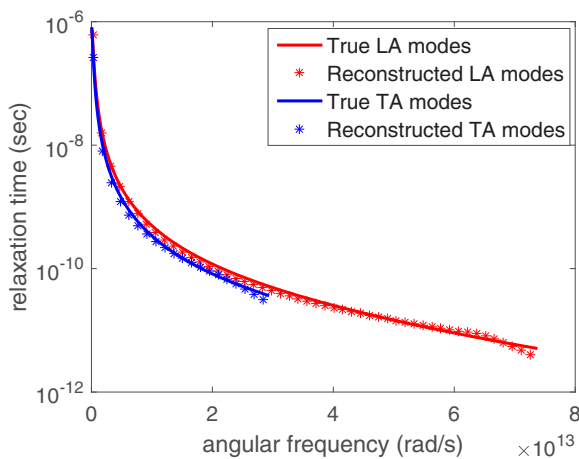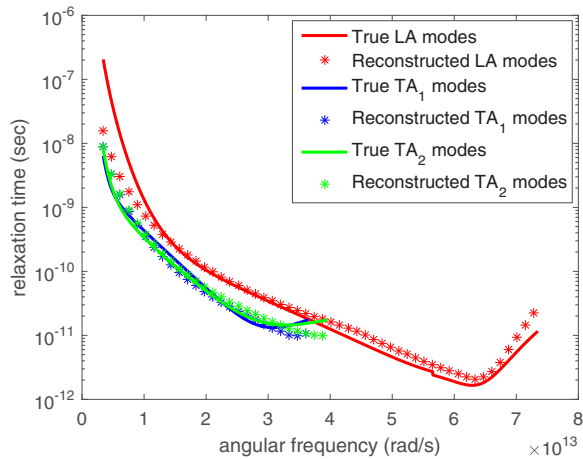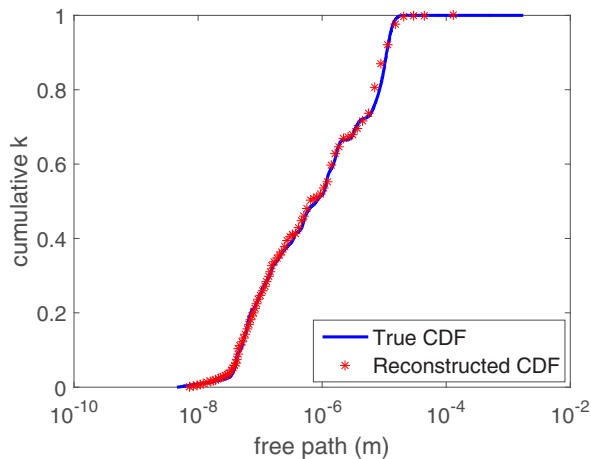

(a) relaxation times

(b) free path distribution

FIG. 7. Comparison between true and reconstructed relaxation times and free path distribution using adjoint MC simulation from noisy synthetic data for the Holland material model.

(a) relaxation times

(b) free path distribution

FIG. 8. Comparison between true and reconstructed relaxation times and free path distribution using IFFT of (10) with the *ab initio* material model.

The reconstructed material properties in the presence of noise ($\mathcal{N}_m = 10^3$) using IFFT of (10) and MC simulation are provided in Figs. 10 and 11, respectively.

We observe that the general level of agreement is very good, but not at the level of the Holland model discussed in Sec. III D 1. This is clearly to be expected given the relative complexity of the two models and the fact that the parametrization (7) is related to the Holland model in limiting cases. We also note that although the discrepancy is particularly noticeable for low frequencies, this is primarily an artifact of the low density of states of modes in these frequency ranges. Specifically, the density of states of the LA modes for $\omega \leqslant 8 \times 10^{12}$ rad/s is zero [i.e., none of the two terms in (8) influences τ_ω^{LA} for $\omega \leqslant 8 \times 10^{12}$ rad/s]. The role of density of states can be further verified by noting that the reconstructed free path distribution is in all cases in better agreement with the input (true) data compared to the corresponding relaxation times.

We also observe that, as in the case of the Holland model, the noise in the synthetic data has only a small effect on the reconstruction quality.

IV. COMPARISON TO EFFECTIVE THERMAL CONDUCTIVITY APPROACH

The accuracy of the reconstruction process shown in Figs. 3, 4, 6–11 is very encouraging and, generally speaking, superior to that obtained by effective-thermal-conductivity-based approaches (see, for example, Fig. 2 in Ref. [7], or Fig. 12 of this paper). In Ref. [7], it is pointed out that the effective-thermal-conductivity-based approach is less accurate outside the range of length scales over which input data is available and thus the discrepancies observed in Ref. [7] may be attributed to the lack of data in the range $L \lesssim 1$ μm and $L \gtrsim 15$ μm. On the other hand, as shown in Fig. 12, reconstruction using the method proposed here using relaxation data for $L =$
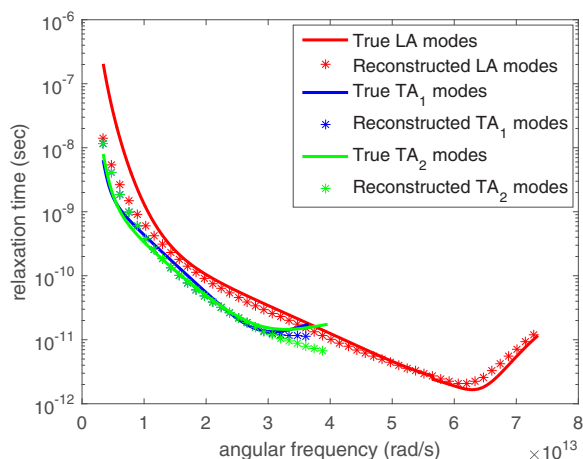
(a) relaxation times
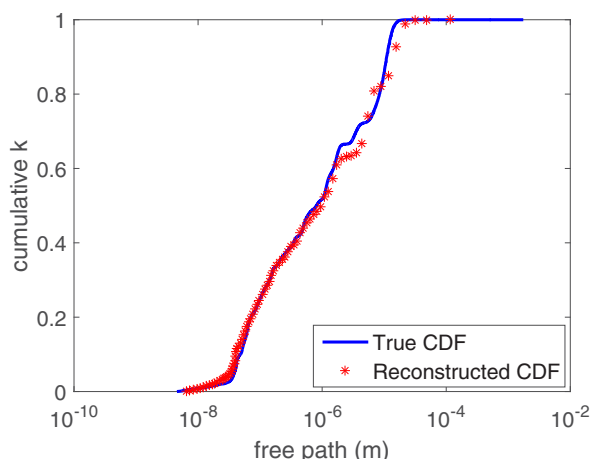
(b) free path distribution

FIG. 9. Comparison between true and reconstructed relaxation times and free path distribution using T_{BTE} obtained from adjoint MC simulation of the *ab initio* material model.
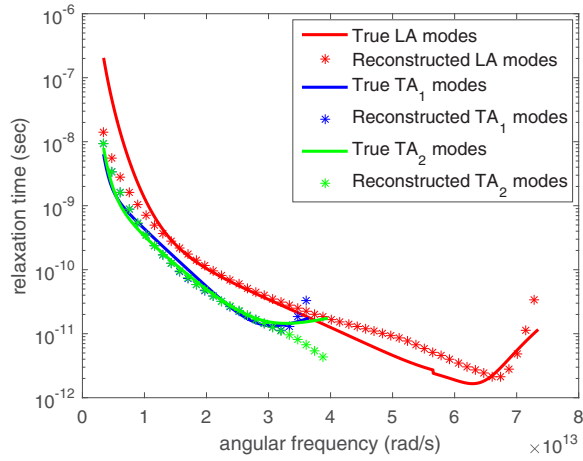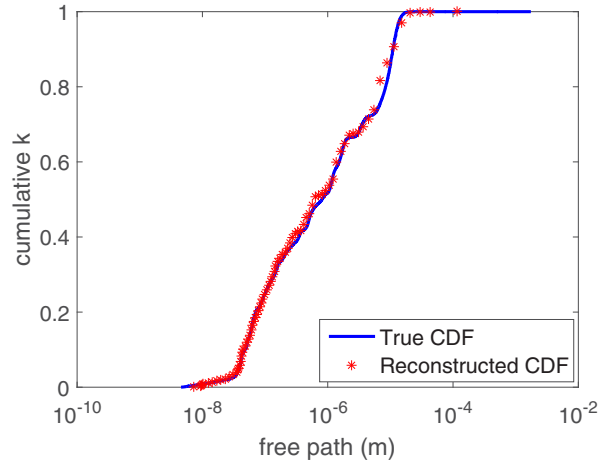
(a) relaxation times

(b) free path distribution

FIG. 10. Comparison between true and reconstructed relaxation times and free path distribution using IFFT of (10) from noisy synthetic data for the *ab initio* material model.

1 μm, 5 μm, 10 μm, and 50 μm, reveals that the proposed method is less sensitive to the range of wavelengths spanned by the input data.

Sensitivity to the range over which input data exists is very important, not only because some length scales may not be experimentally accessible [7], but also because the effective thermal conductivity concept cannot be used to analyze small length scale or early-time data—recall that Fourier-based descriptions are only accurate in the limit of large length scales (compared to the mean-free path) and long timescales (compared to the mean time between scattering events). Below, we theoretically analyze the limitations arising from these requirements by studying in detail the response associated with the TTG setup.

Another problem associated with the effective thermal conductivity approach is that, other than in the thermal grating geometry, the associated suppression functions are unknown (and depend not only on the experimental setup, but also on

the material parameters that are being calculated). Using gray MC simulations as a substitute for the suppression function introduces approximations (see Ref. [17] for a discussion) that are not always acceptable and more importantly not *a priori* controllable.

A. Thermal grating case in detail

Clearly, in order to extract information from the experiment correctly, a model needs to be able to fit the functional form of the experimental response accurately. We now examine, both theoretically and via simulation, if this requirement is satisfied by the effective thermal conductivity formalism in the case of the TTG problem.

We first recall that the effective thermal conductivity concept applies to late times, as defined by $\tau_\omega \zeta \ll 1$ [10] (ζ is the Fourier transform variable with respect to time; see discussion in Sec. III A). Following previous work [10],
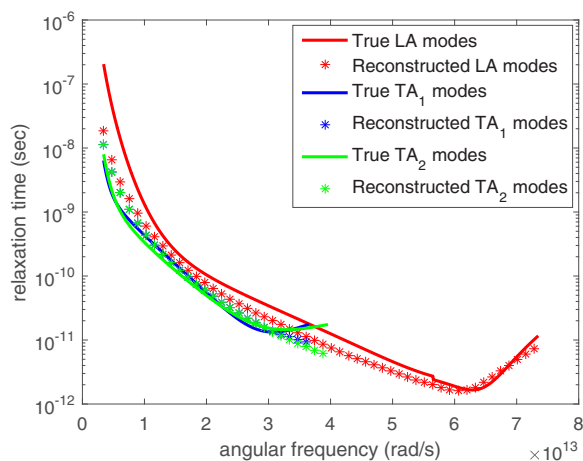
(a) relaxation times
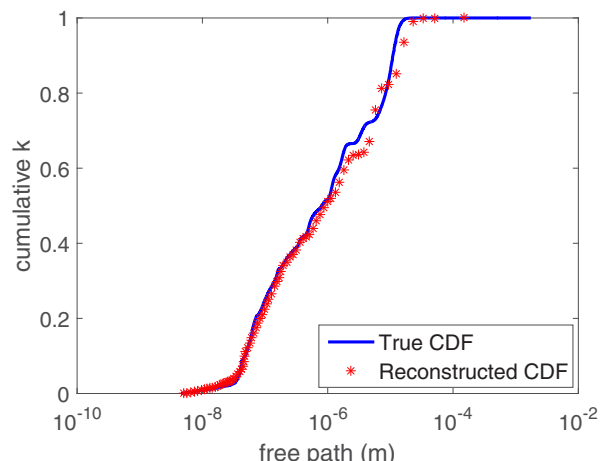
(b) free path distribution

FIG. 11. Comparison between true and reconstructed relaxation times and free path distribution using adjoint MC simulation from noisy synthetic data for the *ab initio* material model.

(a) relaxation times
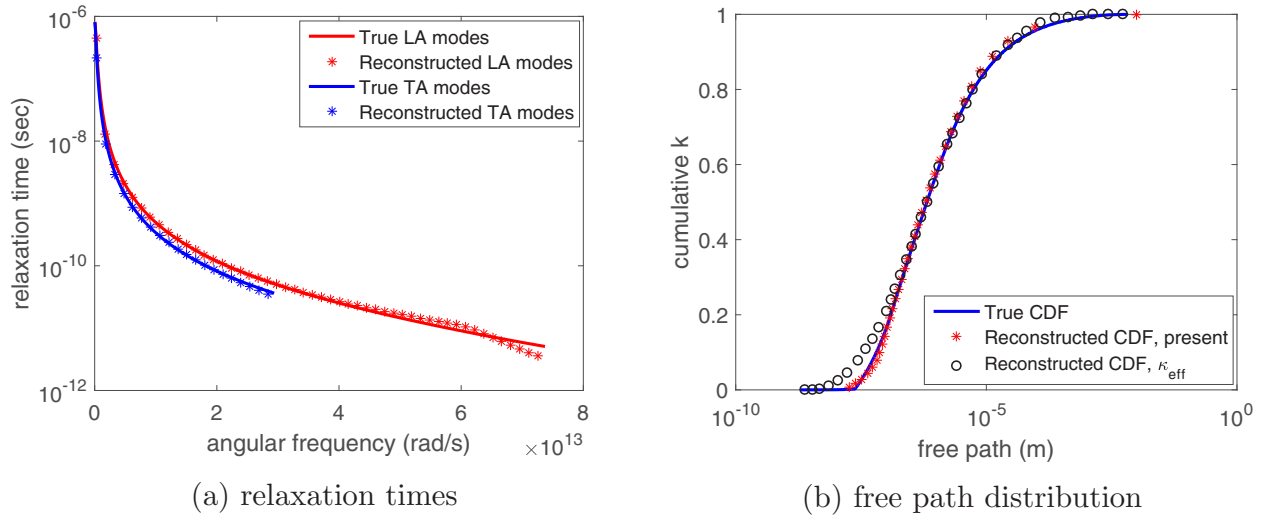

(b) free path distribution

FIG. 12. Comparison between true and reconstructed data for the case of limited range of input wavelengths: (a) Reconstructed relaxation times using IFFT of the semianalytical result (10) for the Holland material model using $L = 1\ \mu$m, $5\ \mu$m, $10\ \mu$m, and $50\ \mu$m. Relaxation data was recorded in the time period $0 \leqslant t \leqslant t_L$, where $t_L = \min(t_{L,1\%}, 50$ ns); (b) Comparison of the free path distribution obtained from reconstruction shown in (a) with data transcribed [39] from Fig. 2 of Ref. [7] (denoted "Reconstructed CDF, κ_{eff}"). The latter was obtained following the effective thermal conductivity approach using 12 relaxation profiles with wavelengths in the range $L = 1$–$15\ \mu$m.

we simplify (11) in the limit of $\tau_\omega \zeta \ll 1$ to obtain (see Appendix C)

$$S_\omega = \frac{C_\omega}{\tau_\omega} \left[\frac{\tan^{-1}(\mathrm{Kn}_\omega)}{\mathrm{Kn}_\omega} - \frac{\tau_\omega}{\mathrm{Kn}_\omega^2 + 1} i\zeta \right]. \quad (12)$$

Here, $\mathrm{Kn}_\omega = 2\pi v_\omega \tau_\omega / L$. Substituting equation (12) in (10) and performing the inverse Fourier transform in time leads to the following temperature response in the late time limit

$t \gg \tau_\omega$

$$\Delta T = A \exp\left(\frac{2\pi i x}{L}\right) \exp\left[-\left(\frac{2\pi}{L}\right)^2 \frac{\kappa_{\mathrm{mod}}}{C_{\mathrm{mod}}} t\right], \quad (13)$$

where

$$\kappa_{\mathrm{mod}} = \int_\omega \frac{1}{3} C_\omega v_\omega^2 \tau_\omega \left\{ \frac{3}{\mathrm{Kn}_\omega^2} \left[1 - \frac{\tan^{-1}(\mathrm{Kn}_\omega)}{\mathrm{Kn}_\omega} \right] \right\} d\omega \quad (14)$$

is the effective thermal conductivity as found before [10],

$$A = \frac{\left[\int_\omega \frac{C_\omega \tau_\omega}{\mathrm{Kn}_\omega^2 + 1} d\omega \int_\omega \frac{C_\omega}{\tau_\omega} \left(1 - \frac{\tan^{-1}(\mathrm{Kn}_\omega)}{\mathrm{Kn}_\omega}\right) d\omega + \int_\omega \frac{C_\omega}{\mathrm{Kn}_\omega^2 + 1} d\omega \int_\omega \frac{C_\omega}{\mathrm{Kn}_\omega} \tan^{-1}(\mathrm{Kn}_\omega) d\omega \right]^2}{\left[\int_\omega \frac{C_\omega}{\mathrm{Kn}_\omega^2 + 1} d\omega \right]^3} \quad (15)$$

is the response amplitude, and

$$C_{\mathrm{mod}} = \int_\omega \frac{C_\omega}{\mathrm{Kn}_\omega^2 + 1} d\omega \quad (16)$$

is an effective heat capacity.

In other words, although the response (13) is of exponential form in time, it is not a solution of the Fourier heat equation with an effective thermal conductivity κ_{mod}, as usually assumed. Response (13) is a diffusive type of solution, which differs from the classical Fourier solution by featuring

(i) an amplitude, A, different from the original temperature perturbation in the TTG experiment (taken to be 1 K here);

(ii) a thermal conductivity given by κ_{mod};

(iii) a heat capacity given by C_{mod}.

Moreover, we always need to keep in mind that the above is only true for $\tau_\omega \zeta \ll 1$, which turns out to have significant implications. Using the fact that $\kappa_{\mathrm{mod}}/C_{\mathrm{mod}} \sim O(\kappa/C) \sim$

$\langle \Lambda_\omega \rangle^2 / \langle \tau_\omega \rangle$ we can write (13) in the form

$$\Delta T \sim A \exp\left(\frac{2\pi i x}{L}\right) \exp\left(-\pi^2 \mathrm{Kn}^2 \frac{t}{\langle \tau_\omega \rangle}\right), \quad (17)$$

where $\mathrm{Kn} = \langle \Lambda_\omega \rangle / L$ is the (average) Knudsen number, $\langle \Lambda_\omega \rangle$ is the mean-free path and $\langle \tau_\omega \rangle$ is the mean-free time. This leads us to conclude that the requirement $t/\tau_\omega \gg 1$ ($t/\langle \tau_\omega \rangle \gg 1$) is incompatible with a solution of this form ($\Delta T \to 0$) unless $\mathrm{Kn}^2 \ll 1$. This mathematical incompatibility is a simple statement of the physical fact that relaxation times scale with the system size and thus for a small system (not satisfying $\mathrm{Kn}^2 \ll 1$) the response timescale will be on the order of the relaxation time or smaller (no experimentally measurable signal will be available at times much longer than the relaxation time)—in other words, no fully diffusive relaxation regime is possible for systems not satisfying $\mathrm{Kn}^2 \ll 1$.

The above discussion is validated in Figs. 13 and 14; the figures compare various Fourier-based relaxation profiles to the BTE solution of the grating relaxation problem for various

(a) Relaxation profile for $L = 10 \ nm$

(b) Relaxation profile for $L = 100 \ nm$

(c) Relaxation profile for $L = 400 \ nm$

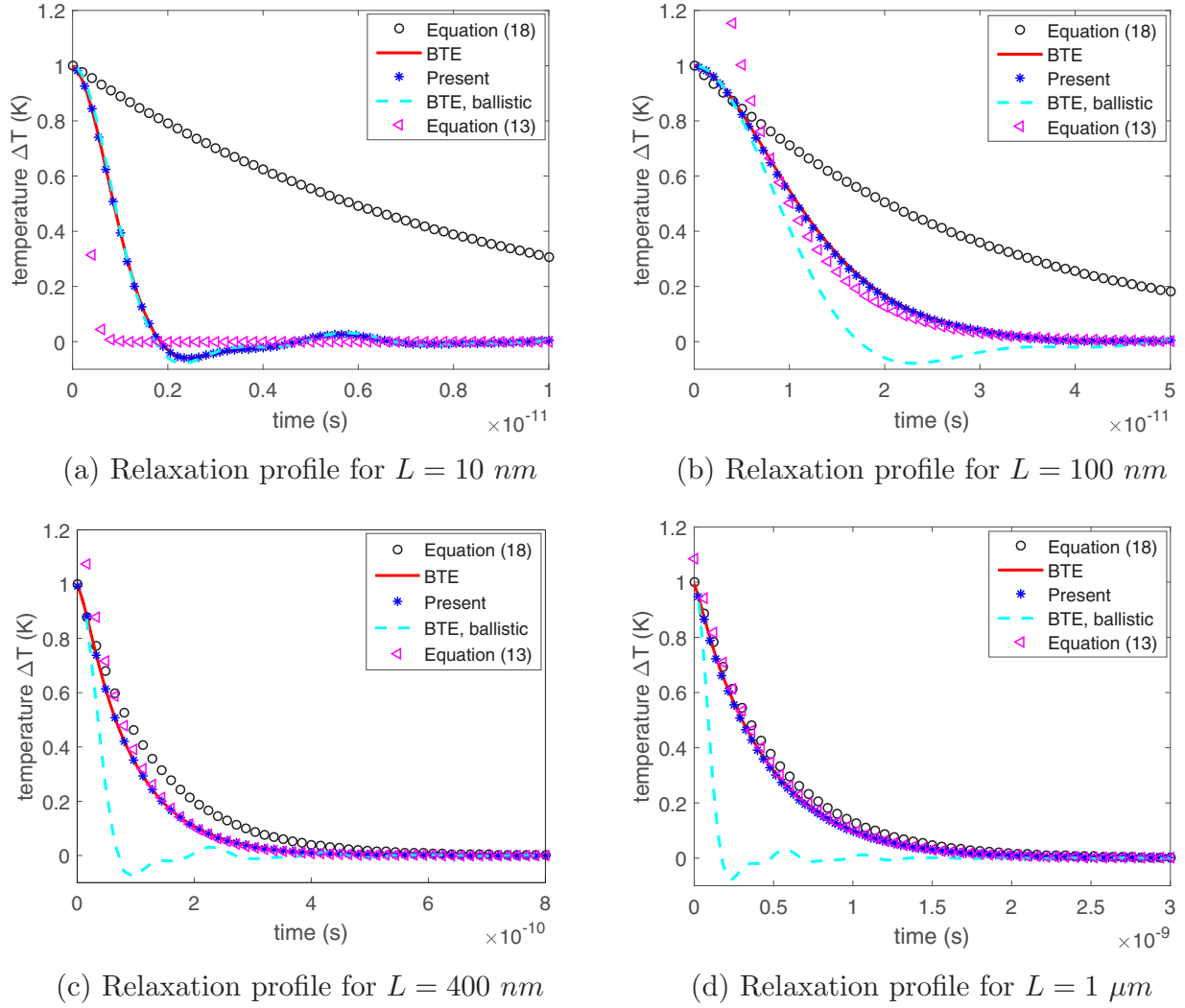(d) Relaxation profile for $L = 1 \ \mu m$

FIG. 13. Comparison between the method proposed in the present paper and various Fourier-based methods. Temperature relaxation profiles are shown for four grating wavelengths and compared to BTE solution for the *ab initio* material model (denoted "BTE"). The prediction of the method proposed here, denoted as "present", is given by solution of the Boltzmann equation based on the reconstructed relaxation time data of Fig. 8. Solutions based on Eqs. (13) and (18) are denoted "Equation (13)" and "Equation (18)", respectively.

values of the wavelength L. In addition to solution (13), we also consider the traditional effective thermal conductivity approach given by [10],

$$\Delta T = \exp\left(\frac{2\pi i x}{L}\right) \exp\left(-\left(\frac{2\pi}{L}\right)^2 \frac{\kappa_{\mathrm{mod}}}{C} t\right). \quad (18)$$

The figures also show the solution of the same problem obtained via IFFT of (10) using the reconstructed τ_ω data (as shown in Fig. 3 for the Holland model and Fig. 8 for the *ab initio* model). Figure 13 shows results for the *ab initio* material model ($\langle \Lambda_\omega \rangle = 95.7$ nm) and Fig. 14 for the Holland model ($\langle \Lambda_\omega \rangle = 85.5$ nm). Here, $\langle \Lambda_\omega \rangle$ was calculated using the procedure outlined in Ref. [40].

In both figures, we observe that the BTE solution based on reconstructed relaxation times, referred to as "present", is the only solution that is able to predict the correct temperature profiles [IFFT of (10), denoted by "BTE"] in all Kn regimes, for all times. Referring to Fig. 13, at $L = 10$ nm, the ballistic

solution of the BTE (provided in Appendix D) is also able to predict the temperature profile, although for $t \gtrsim 1.5$ ps some discrepancies are observable (scattering is no longer completely negligible); Fourier-based approximations are inaccurate. For $L = 100$ nm (Kn ≈ 0.96), none of the Fourier-based approximations are able to predict the correct temperature profile; although solution (13) provides a significantly better approximation compared to expression (18) at late times, the BTE solution is clearly not of exponential form at early and moderate times [in other words, although (13) appears to be close to the BTE solution, this is partly because both go to 0 at late times]. At $L = 400$ nm (Kn ≈ 0.24) the agreement between (13) and the BTE solution is good; Eq. (18) remains inaccurate. The comparison at $L = 1 \ \mu m$ (Kn ≈ 0.096) shows good agreement between Eq. (13) and the BTE solution; Eq. (18) also becomes a reasonable approximation. Further comparison (not shown here) shows that at $L = 10 \ \mu m$ (Kn ≈ 0.0096), both Fourier-based solutions are able to reproduce the Boltzmann solution.

(a) Relaxation profile for $L = 10\ nm$

(b) Relaxation profile for $L = 100\ nm$

(c) Relaxation profile for $L = 400\ nm$

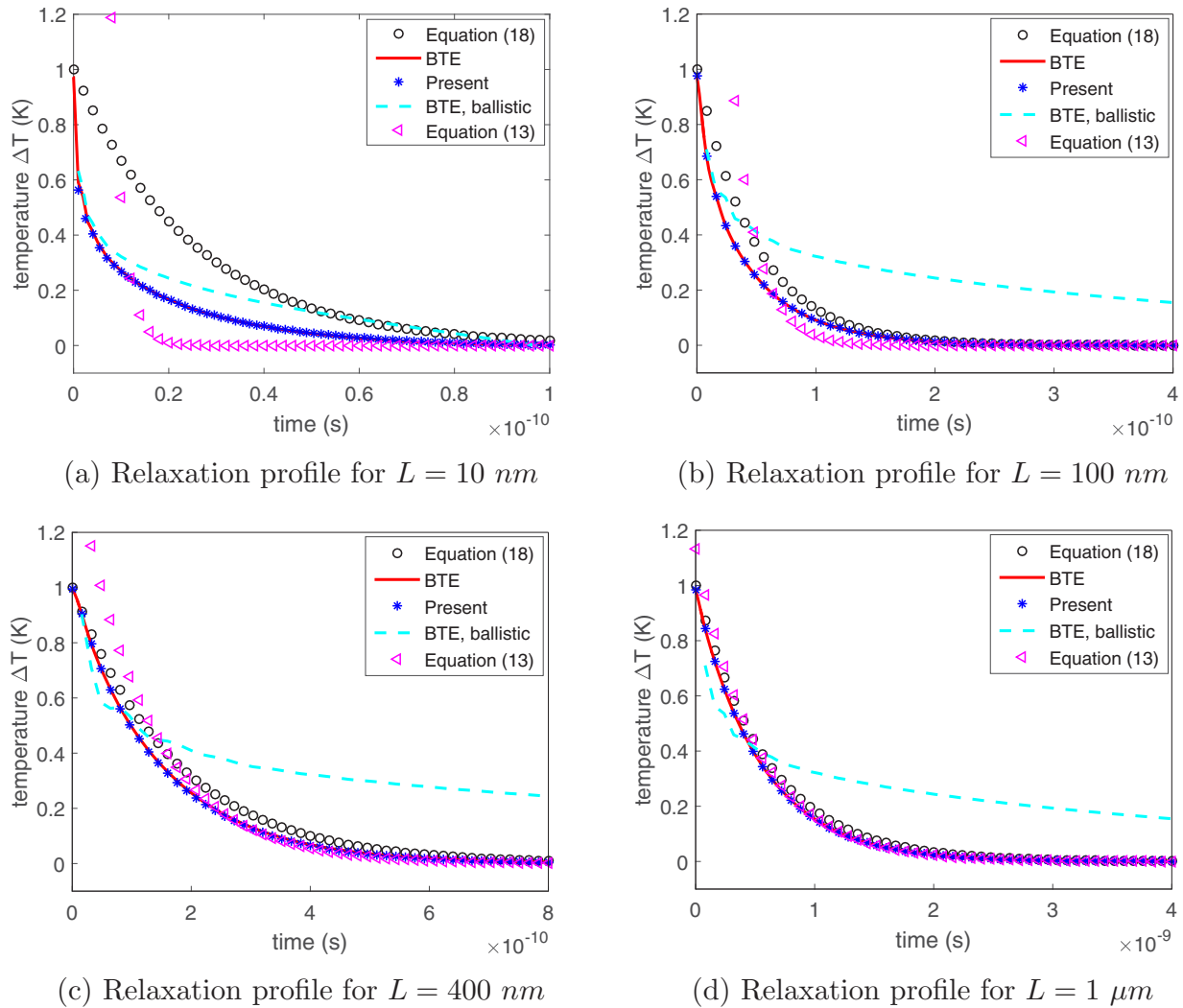(d) Relaxation profile for $L = 1\ \mu m$

FIG. 14. Comparison between the method proposed in the present paper and various Fourier-based methods. Temperature relaxation profiles are shown for four grating wavelengths and compared to BTE solution for the Holland material model (denoted "BTE"). The prediction of the method proposed here, denoted as "present", is given by solution of the Boltzmann equation based on the reconstructed relaxation time data of Fig. 3. Solutions based on Eqs. (13) and (18) are denoted "Equation (13)" and "Equation (18)", respectively.

A comparison for the Holland model can be found in Fig. 14. The results are similar, but generally reveal worse performance by Eq. (13) in the critical Kn = 0.2–1 range. Also, the ballistic behavior is observed at smaller wavelengths (approximately $L = 1$ nm, not shown here).

In summary, although relation (13) shows that a regime featuring exponential relaxation is possible, this is only physically realizable (and measurable) for $\mathrm{Kn}^2 \ll 1$. This is clearly more favorable than the typical requirement (Kn $\ll$ 1 for homogeneous materials, Kn $\lll$ 1 in the presence of boundaries [41]) for validity of Fourier's law uncorrected; the improved range of validity is due to the corrections (14)–(16), which are available, in part, due to the simplicity of the TTG problem and geometry. Although extensions of Fourier approaches are sometimes possible (e.g., see Ref. [41] for the role of boundaries), these are not always guaranteed to exist or be tractable and their range of validity cannot be expected to extend to Kn $\sim$ 1, except fortuitously.

With the above considered, for the TTG case, the effective thermal conductivity construction and associated solution (13) is only strictly theoretically justified in the limit $\mathrm{Kn}^2 \ll 1$. In some cases this coincides with the range in which experiments operate [5], in which case reconstruction using a diffusive approximation may be acceptable provided:

(i) the correct asymptotic relation [i.e., Eq. (13)] is used;

(ii) some loss of accuracy outside the range over which experimental data is available is acceptable.

We also point out that the validation in Ref. [7] featured wavelengths satisfying $\mathrm{Kn}^2 \ll 1$. In general, however, the requirements $\mathrm{Kn}^2 \ll 1$ and $t \gg \tau_\omega$ are very restrictive, especially when considering that typical pump-probe response time is on the order of a few nanoseconds [8]. In contrast, the method proposed here introduces no length scale or timescale restriction; moreover, if input data is available over a limited range of wavelengths, the quality of the reconstruction does not suffer significantly.

V. SUMMARY AND OUTLOOK

By analyzing the TTG response in detail we have shown that, as expected, reconstruction using the effective thermal conductivity concept is limited to late (compared to the mean-free time) times and large (compared to the mean-free path) length scales ($\text{Kn}^2 \ll 1$ for the TTG in particular). Using input data that does not satisfy these requirements will lead to reconstruction error; on the other hand, using data in a limited range of characteristic length scales also leads to reconstruction error [7].

In this paper we have proposed an alternative approach to the reconstruction problem that avoids the limitations associated with the effective thermal conductivity approach. The proposed method assumes knowledge of the phonon group velocities and poses the reconstruction as an optimization problem seeking the function τ_ω that minimizes the discrepancy between the observed experimental data and the solution of the BTE as applied to the experimental process. Although much research and improvements remain to be made, one of the main contributions of the present paper is to show that reconstruction based on a more rigorous foundation (which does not make use of the assumption of Fourier behavior) is possible.

The proposed formulation is sufficiently general to accept solutions of the BTE obtained by any means. In fact, we envision applications to problems including interfaces between materials [42] (and where the reconstruction will include inference of interface properties) as direct extensions of the present work.

The optimization process is achieved by the Nelder-Mead algorithm that does not require gradient calculation and is thus robust to noise. Our results verify that reconstruction is robust both in the presence of noise in the input (experimental) data and the BTE solutions when the latter are obtained by MC simulation. Although MC simulations are considerably more expensive, they are, in fact, the more relevant to applications of practical interest (e.g., Ref. [8]), which are in general high dimensional and not expected to lend themselves to analytical solutions. The cost of MC simulations is partially mitigated by their excellent parallel efficiency. Moreover, in cases where the experimental measurement is limited to one (or a few) discrete spatial locations, the MC simulation cost can be made independent of dimensionality using techniques such as adjoint formulations.

Our validation tests started from multiple distinct initial conditions thus subjecting the optimization process to a worst-case scenario, since in most cases some *a priori* information on the nature of the solution is expected to exist. In the present case, the lack of prior information was overcome by starting the optimization process, as a first stage, from a sweep of different initial conditions and choosing the result with the lowest objective function value as the initial condition for a second optimization stage. In the case of MC simulations, this approach was possible due to the robustness of the NM algorithm to noise, which enabled us to perform the first two stages of calculations using very cheap (noisy) simulations. In general, *a priori* information could be very useful in ensuring convergence to the correct solution, which due to the highly nonconvex nature of the minimization problem is not guaranteed. Future research will focus on formulations which exploit *a priori* information on the nature of the solution as well as alternative optimization algorithms to improve convergence rates and accuracy.

Our results also show that the reconstruction process is very robust with respect to the time window over which the material response is observed, in contrast to Fourier-based approaches, which assume a late-time response. More specifically, by matching the material response to BTE solutions, the reconstruction is successful with response data limited to very early times (e.g., on the order of 5 nanoseconds) that are typical in pump-probe experiments [8] but do not satisfy assumptions required for diffusive behavior to set in. Validation of the proposed methodology using experimental data of thermal relaxation processes will be studied in the near future.

APPENDIX A: PARAMETERS OF PIECEWISE LINEAR MODEL

Relationship (7) is constructed such that the intersections of the piecewise linear segments at ω_j^S, $j = 1, \ldots, M - 1$, are smoothed by third-order polynomial functions. Each smoothing polynomial extends over a frequency range of 2Δ, centered on ω_j^S and denoted by (X_{2j-1}^S, X_{2j}^S), where

$$X_0^S = \omega_0^S, \quad X_{2j}^S = \omega_j^S + \Delta, \quad X_{2j-1}^S = \omega_j^S - \Delta, \quad j \in \{1, \ldots, M-1\}, \quad X_{2M-1}^S = \omega_M^S. \tag{A1}$$

In this work, we have used $\Delta = 5 \times 10^{12}$ rad/s.

The coefficients a_j^S, b_j^S, c_j^S, and d_j^S are calculated from the following equations:

$$a_j^S = -\frac{\log\left(1 - \left(\frac{\Delta}{\omega_j^S}\right)^2\right)}{\left[\log\left(\frac{\omega_j^S + \Delta}{\omega_j^S - \Delta}\right)\right]^3}\left[\frac{\log\left(\frac{\tau_{\omega_{j+1}}^S}{\tau_{\omega_j}^S}\right)}{\log\left(\frac{\omega_{j+1}^S}{\omega_j^S}\right)} - \frac{\log\left(\frac{\tau_{\omega_j}^S}{\tau_{\omega_{j-1}}^S}\right)}{\log\left(\frac{\omega_j^S}{\omega_{j-1}^S}\right)}\right],$$

$$b_j^S = 0.5 \left\{ \frac{1}{\log\left(\frac{\omega_j^S + \Delta}{\omega_j^S - \Delta}\right)} \left[\frac{\log\left(\frac{\tau_{\omega_{j+1}}^S}{\tau_{\omega_j}^S}\right)}{\log\left(\frac{\omega_{j+1}^S}{\omega_j^S}\right)} - \frac{\log\left(\frac{\tau_{\omega_j}^S}{\tau_{\omega_{j-1}}^S}\right)}{\log\left(\frac{\omega_j^S}{\omega_{j-1}^S}\right)} \right] - 3a_j^S \log\left((\omega_j^S)^2 - \Delta^2\right) \right\},$$

$$c_j^S = \frac{\log\left(\frac{\tau_{\omega_j}^S}{\tau_{\omega_{j-1}}^S}\right)}{\log\left(\frac{\omega_j^S}{\omega_{j-1}^S}\right)} - 3a_j^S \left[\log\left(\omega_j^S - \Delta\right)\right]^2 - 2b_j^S \log\left(\omega_j^S - \Delta\right),$$

$$d_j^S = \log\left(\tau_{\omega_{j-1}}^S\right) - \log\left(\omega_{j-1}^S\right) \frac{\log\left(\frac{\tau_{\omega_j}^S}{\tau_{\omega_{j-1}}^S}\right)}{\log\left(\frac{\omega_j^S}{\omega_{j-1}^S}\right)} + 0.5 \frac{\left[\log\left(\omega_j^S - \Delta\right)\right]^2}{\log\left(\frac{\omega_j^S + \Delta}{\omega_j^S - \Delta}\right)} \left[\frac{\log\left(\frac{\tau_{\omega_{j+1}}^S}{\tau_{\omega_j}^S}\right)}{\log\left(\frac{\omega_{j+1}^S}{\omega_j^S}\right)} - \frac{\log\left(\frac{\tau_{\omega_j}^S}{\tau_{\omega_{j-1}}^S}\right)}{\log\left(\frac{\omega_j^S}{\omega_{j-1}^S}\right)} \right]$$

$$- 0.5a_j^S \left[\log\left(\omega_j^S - \Delta\right)\right]^2 \left[3 \log\left(\omega_j^S + \Delta\right) - \log\left(\omega_j^S - \Delta\right)\right], \tag{A2}$$

where $j \in \{1, \ldots, M-1\}$ and $S \in \{LA, TA_1, TA_2\}$.

APPENDIX B: SEMIANALYTICAL SOLUTION FOR THE TRANSIENT THERMAL GRATING

Here, we derive the semianalytical frequency-domain solution (10) used in Sec. III A using Fourier transform in the frequency domain (with respect to the time variable) and wave-number domain (with respect to the space variable). We will use the subscript ζ to denote the former and the subscript η to denote the latter. By applying a Fourier transform to (9) in both variables we obtain

$$i\zeta e_{\zeta\eta}^d + i\eta v_\omega \cos(\theta) e_{\zeta\eta}^d = -\frac{1}{\tau_\omega} e_{\zeta\eta}^d + \frac{1}{\tau_\omega} (de^{eq}/dT)_{T_{eq}} \Delta\widetilde{T}_{\zeta\eta} + 2\pi (de^{eq}/dT)_{T_{eq}} \delta(\eta - 2\pi L^{-1}), \tag{B1}$$

which provides the following relationship for $e_{\zeta\eta}^d$

$$e_{\zeta\eta}^d = \frac{(de^{eq}/dT)_{T_{eq}} \left[\tau_\omega^{-1} \Delta\widetilde{T}_{\zeta\eta} + 2\pi \delta(\eta - 2\pi L^{-1})\right]}{i\zeta + i\eta v_\omega \cos(\theta) + \tau_\omega^{-1}}. \tag{B2}$$

Applying Fourier transform in both variables to Eq. (3) and replacing $e_{\zeta\eta}^d$ with the above result, we obtain the following expression for $\Delta\widetilde{T}_{\zeta\eta}$:

$$\int_{\mathbf{\Omega}} \int_\omega \left[\frac{C_\omega}{\tau_\omega} \Delta\widetilde{T}_{\zeta\eta} - \frac{(de^{eq}/dT)_{T_{eq}} \left[\tau_\omega^{-1} \Delta\widetilde{T}_{\zeta\eta} + 2\pi \delta(\eta - 2\pi L^{-1})\right]}{i\tau_\omega\zeta + i\eta v_\omega\tau_\omega \cos(\theta) + 1} D_\omega \right] d\omega d\mathbf{\Omega} = 0, \tag{B3}$$

which after integrating over $\theta \in (0, \pi)$ and $\phi \in (0, 2\pi)$ and algebraic simplification leads to the following relationship:

$$\Delta\widetilde{T}_{\zeta\eta} = \frac{\frac{\pi\delta(\eta - 2\pi L^{-1})}{\eta} \int_\omega \frac{iC_\omega}{v_\omega\tau_\omega} \ln\left(\frac{\tau_\omega\zeta - v_\omega\tau_\omega\eta - i}{\tau_\omega\zeta + v_\omega\tau_\omega\eta - i}\right) d\omega}{\int_\omega \frac{C_\omega}{\tau_\omega} d\omega - \frac{1}{2\eta} \int_\omega \frac{iC_\omega}{v_\omega\tau_\omega^2} \ln\left(\frac{\tau_\omega\zeta - v_\omega\tau_\omega\eta - i}{\tau_\omega\zeta + v_\omega\tau_\omega\eta - i}\right) d\omega}. \tag{B4}$$

Equation (B4) can be further simplified by applying the inverse Fourier transform in wave-number domain η. Noting that Eq. (B4) is in the form of $\Delta\widetilde{T}_{\zeta\eta} = \delta(\eta - 2\pi L^{-1}) G(\eta, \zeta)$, we use the identity

$$\frac{1}{2\pi} \int_{-\infty}^\infty \delta(\eta - 2\pi L^{-1}) G(\eta, \zeta) e^{i\eta x} d\eta = \frac{1}{2\pi} G(2\pi L^{-1}, \zeta) e^{2\pi ix/L}, \tag{B5}$$

to obtain

$$\Delta\widetilde{T}_\zeta = \frac{e^{2\pi ix/L} \int_\omega S_\omega \tau_\omega d\omega}{\int_\omega \left[C_\omega \tau_\omega^{-1} - S_\omega\right] d\omega}, \tag{B6}$$

where S_ω is given in (11). Equation (B6) is similar to the result obtained in Ref. [10].

To obtain an expression for the temperature, we insert (B4) into (B2) and apply the inverse Fourier transform in wave-number domain using the identity (B5) to obtain

$$e_\zeta^d = \frac{e^{2\pi ix/L} (de^{eq}/dT)_{T_{eq}}}{i\tau_\omega\zeta + iv_\omega\tau_\omega \cos(\theta) 2\pi L^{-1} + 1} \left[\frac{\int_\omega S_\omega \tau_\omega d\omega}{\int_\omega C_\omega \tau_\omega^{-1} d\omega - \int_\omega S_\omega d\omega} + 1 \right]. \tag{B7}$$

This relation is then substituted in

$$\int_{\mathbf{\Omega}} \int_\omega \left[C_\omega \Delta T_\zeta - e_\zeta^d D_\omega \right] d\omega d\mathbf{\Omega} = 0, \tag{B8}$$

obtained by applying Fourier transform in the frequency domain to (4). Solving the resulting equation for ΔT_ζ leads to the expression provided in (10).

APPENDIX C: SOLUTION OF THE TRANSIENT THERMAL GRATING FOR LATE TIMES

Introducing the definition $\mathrm{Kn}_\omega = v_\omega \tau_\omega 2\pi L^{-1}$ in Eq. (11), provides the following relationship for S_ω

$$S_\omega = \frac{iC_\omega}{2\mathrm{Kn}_\omega \tau_\omega} \ln \left(\frac{\tau_\omega \zeta - \mathrm{Kn}_\omega - i}{\tau_\omega \zeta + \mathrm{Kn}_\omega - i} \right). \tag{C1}$$

Using a Taylor expansion for $\tau_\omega \zeta \ll 1$ of the logarithmic term in (C1) we obtain

$$S_\omega = \frac{iC_\omega}{2\mathrm{Kn}_\omega \tau_\omega} \left[-2i \tan^{-1}(\mathrm{Kn}_\omega) - \frac{2\mathrm{Kn}_\omega \tau_\omega}{\mathrm{Kn}_\omega^2 + 1} \zeta + O(\tau_\omega^2 \zeta^2) \right], \tag{C2}$$

which is the same expression provided in Eq. (12). If we substitute S_ω in (10) with (C2) and neglect terms of $O(\tau_\omega^2 \zeta^2)$ we obtain

$$\Delta T_\zeta = \frac{e^{2\pi ix/L}}{C} \left\{ \int_\omega C_\omega \tau_\omega \left[\frac{\tan^{-1}(\mathrm{Kn}_\omega)}{\mathrm{Kn}_\omega} - \frac{\tau_\omega i\zeta}{\mathrm{Kn}_\omega^2 + 1} \right] d\omega + \frac{\left[\int_\omega C_\omega \left(\frac{\tan^{-1}(\mathrm{Kn}_\omega)}{\mathrm{Kn}_\omega} - \frac{\tau_\omega i\zeta}{\mathrm{Kn}_\omega^2 + 1} \right) d\omega \right]^2}{\int_\omega \frac{C_\omega}{\tau_\omega} \left[1 - \frac{\tan^{-1}(\mathrm{Kn}_\omega)}{\mathrm{Kn}_\omega} + \frac{\tau_\omega i\zeta}{\mathrm{Kn}_\omega^2 + 1} \right] d\omega} \right\}. \tag{C3}$$

Equation (C3) is in the general form of

$$\Delta T_\zeta = k_1 - k_2 i\zeta + \frac{(k_3 - k_4 i\zeta)^2}{k_5 + k_6 i\zeta}, \tag{C4}$$

where $k_1, k_2, \ldots, k_6$ are independent of Fourier transform variable ζ and depend only on the geometry and the material properties. Equation (C4) can be further simplified in the following form

$$\Delta T_\zeta = k_1 - \frac{k_4^2 k_5}{k_6^2} - \frac{2k_3 k_4}{k_6} + \left(\frac{k_4^2}{k_6} - k_2 \right) i\zeta + \frac{(k_4 k_5 + k_3 k_6)^2}{k_6^2 (k_5 + k_6 i\zeta)}. \tag{C5}$$

Applying inverse Fourier transform to (C5) leads to the following result:

$$\Delta T = \left(k_1 - \frac{k_4^2 k_5}{k_6^2} - \frac{2k_3 k_4}{k_6} \right) \delta(t) + \left(\frac{k_4^2}{k_6} - k_2 \right) \delta'(t) + \frac{(k_4 k_5 + k_3 k_6)^2}{k_6^3} u(t) e^{-\frac{k_5}{k_6} t}, \tag{C6}$$

where $\delta(t)$ and $\delta'(t)$ are the Dirac δ function and its first derivative, respectively, and $u(t)$ is the Heaviside function. At late times (more precisely, $t > 0$), only the last term of (C6) is nonzero. Substituting constants k_1 through k_6 in (C6) with their equivalents from Eq. (C3) leads to the result provided in (13).

APPENDIX D: ANALYTICAL SOLUTION FOR TRANSIENT THERMAL GRATING IN BALLISTIC LIMIT

The temperature relaxation profile in the ballistic limit can be obtained by setting $\tau_\omega \to \infty$ in Eqs. (10) and (11). Using this substitution, for S_ω we have

$$S_\omega = \frac{iC_\omega L}{4\pi v_\omega \tau_\omega^2} \ln \left(\frac{\zeta - v_\omega 2\pi L^{-1}}{\zeta + v_\omega 2\pi L^{-1}} \right). \tag{D1}$$

Substituting this expression in (10), we observe that the second term of (10) vanishes in this limit [the numerator is $O(\tau_\omega^{-2})$, while the denominator is $O(\tau_\omega^{-1})$]. Therefore, we have

$$\Delta T_\zeta = \frac{iLe^{2\pi ix/L}}{4\pi C} \int_\omega \frac{C_\omega}{v_\omega} \ln \left(\frac{\zeta - v_\omega 2\pi L^{-1}}{\zeta + v_\omega 2\pi L^{-1}} \right) d\omega. \tag{D2}$$

The inverse Fourier transform of (D2) can be calculated analytically [43] and gives

$$\Delta T = \frac{Le^{2\pi ix/L}}{2\pi Ct} \int_\omega \frac{C_\omega}{v_\omega} \sin(v_\omega 2\pi L^{-1} t) d\omega. \tag{D3}$$

[1] A. A. Balandin, S. Ghosh, W. Bao, I. Calizo, D. Teweldebrhan, F. Miao, and C. Ning Lau, Superior thermal conductivity of single-layer graphene, Nano Lett. **8**, 902 (2008).

[2] Y. K. Koh and D. G. Cahill, Frequency dependence of the thermal conductivity of semiconductor alloys, Phys. Rev. B **76**, 075207 (2007).

[3] F. Yang and C. Dames, Heating-frequency-dependent thermal conductivity: An analytical solution from diffusive to ballistic regime and its relevance to phonon scattering measurements, Phys. Rev. B **91**, 165311 (2015).

[4] K. T. Regner, A. J. H. McGaughey, and J. A. Malen, Analytical interpretation of nondiffusive phonon transport in thermoreflectance thermal conductivity measurements, Phys. Rev. B **90**, 064302 (2014).

[5] A. A. Maznev, J. A. Johnson, and K. A. Nelson, Onset of nondiffusive phonon transport in transient thermal grating decay, Phys. Rev. B **84**, 195206 (2011).

[6] A. J. Minnich, J. A. Johnson, A. J. Schmidt, K. Esfarjani, M. S. Dresselhaus, K. A. Nelson, and G. Chen, Thermal Conductivity Spectroscopy Technique to Measure Phonon Mean Free Paths, Phys. Rev. Lett. **107**, 095901 (2011).

[7] A. J. Minnich, Determining Phonon Mean Free Paths from Observations of Quasiballistic Thermal Transport, Phys. Rev. Lett. **109**, 205901 (2012).

[8] Y. Hu, L. Zeng, A. J. Minnich, M. S. Dresselhaus, and G. Chen, Spectral mapping of thermal conductivity through nanoscale ballistic transport, Nature Nanotechnology **10**, 701 (2015).

[9] V. Chiloyan, L. Zeng, S. Huberman, A. A. Maznev, K. A. Nelson, and G. Chen, Variational approach to extracting the phonon mean free path distribution from the spectral Boltzmann transport equation, Phys. Rev. B **93**, 155201 (2016).

[10] C. Hua and A. J. Minnich, Transport regimes in quasiballistic heat conduction, Phys. Rev. B **89**, 094302 (2014).

[11] L. Zeng and G. Chen, Disparate quasiballistic heat conduction regimes from periodic heat sources on a substrate, J. Appl. Phys. **116**, 064307 (2014).

[12] A. J. Minnich, Multidimensional quasiballistic thermal transport in transient grating spectroscopy, Phys. Rev. B **92**, 085203 (2015).

[13] J.-P. M. Péraud and N. G. Hadjiconstantinou, Efficient simulation of multidimensional phonon transport using energy-based variance-reduced Monte Carlo formulations, Phys. Rev. B **84**, 205331 (2011).

[14] J.-P. M. Péraud and N. G. Hadjiconstantinou, An alternative approach to efficient simulation of micro/nanoscale phonon transport, Appl. Phys. Lett. **101**, 153114 (2012).

[15] J.-P. M. Péraud, C. D. Landon, and N. G. Hadjiconstantinou, Monte Carlo methods for solving the Boltzmann transport equation, Ann. Rev. Heat Transfer **17**, 205 (2014).

[16] J.-P. M. Péraud and N. G. Hadjiconstantinou, Adjoint-based deviational Monte Carlo methods for phonon transport calculations, Phys. Rev. B **91**, 235321 (2015).

[17] K. C. Collins, A. A. Maznev, Z. Tian, K. Esfarjani, K. A. Nelson, and G. Chen, Non-diffusive relaxation of a transient thermal grating analyzed with the Boltzmann transport equation, J. Appl. Phys. **114**, 104302 (2013).

[18] S. Bernard, E. Whiteway, V. Yu, D. G. Austing, and M. Hilke, Probing the experimental phonon dispersion of graphene using ^{12}C and ^{13}C isotopes, Phys. Rev. B **86**, 085409 (2012).

[19] F. Widulle, T. Ruf, O. Buresch, A. Debernardi, and M. Cardona, Raman Study of Isotope Effects and Phonon Eigenvectors in SiC, Phys. Rev. Lett. **82**, 3089 (1999).

[20] J. Serrano, J. Strempfer, M. Cardona, M. Schwoerer-Böhning, H. Requardt, M. Lorenzen, B. Stojetz, P. Pavone, and W. J. Choyke, Determination of the phonon dispersion of zinc blende (3C) silicon carbide by inelastic x-ray scattering, Appl. Phys. Lett. **80**, 4360 (2002).

[21] J. Maultzsch, S. Reich, C. Thomsen, E. Dobardžić, I. Milošević, and M. Damnjanović, Phonon dispersion of carbon nanotubes, Solid State Commun. **121**, 471 (2002).

[22] A. Eichler, K.-P. Bohnen, W. Reichardt, and J. Hafner, Phonon dispersion relation in rhodium: Ab initio calculations and neutron-scattering investigations, Phys. Rev. B **57**, 324 (1998).

[23] T. Luo, J. Garg, J. Shiomi, K. Esfarjani, and G. Chen, Gallium arsenide thermal conductivity and optical phonon relaxation times from first-principles calculations, Europhys. Lett. **101**, 16001 (2013).

[24] L. Wirtz and A. Rubio, The phonon dispersion of graphite revisited, Solid State Commun. **131**, 141 (2004).

[25] P. Scharoch, K. Parliński, and A. Kiejna, Ab initio calculations of phonon dispersion relations in aluminum, Acta Phys. Pol. A **97**, 349 (2000).

[26] A. S. Henry and G. Chen, Spectral phonon transport properties of silicon based on molecular dynamics simulations and lattice dynamics, J. Comput. Theor. Nanoscience **5**, 141 (2008).

[27] M. G. Holland, Analysis of lattice thermal conductivity, Phys. Rev. **132**, 2461 (1963).

[28] J. A. Nelder and R. Mead, A simplex method for function minimization, Comput. J. **7**, 308 (1965).

[29] K. Klein and J. Neira, Nelder-Mead simplex optimization routine for large-scale problems: A distributed memory implementation, Computat. Econ. **43**, 447 (2014).

[30] M. Mitchell, *An Introduction to Genetic Algorithms* (MIT Press, Cambridge, 1998).

[31] S. Kirkpatrick, C. D. Gelatt, and M. P. Vecchi, Optimization by simulated annealing, Science **220**, 671 (1983).

[32] J. C. Lagarias, J. A. Reeds, M. H. Wright, and P. E. Wright, Convergence properties of the Nelder-Mead simplex method in low dimensions, SIAM J. Optim. **9**, 112 (1998).

[33] W. H. Press, S. A. Teukolsky, W. T. Vetterling, and B. P. Flannery, *Numerical Recipes in C: The Art of Scientific Computing* (Cambridge University Press, Cambridge, 1992).

[34] R. R. Barton and J. S. Ivey Jr., *Proceedings of the 23rd Winter Simulation Conference* (IEEE, 1991).

[35] J. A. Rogers, Y. Yang, and K. A. Nelson, Elastic modulus and in-plane thermal diffusivity measurements in thin polyimide films using symmetry-selective real-time impulsive stimulated thermal scattering, Appl. Phys. A **58**, 523 (1994).

[36] A. J. Minnich, Ph.D. thesis, Massachusetts Institute of Technology, 2011.

[37] E. O. Brigham, *The Fast Fourier Transform* (Prentice-Hall, Upper Saddle River, New Jersey, 1988).

[38] N. G. Hadjiconstantinou, Hybrid atomistic-continuum formulations and the moving contact-line problem, J. Comput. Phys. **154**, 245 (1999).

[39] Due to a small discrepancy between the true data of Ref. [7] and the present work (likely related to discretization), the "Reconstructed CDF, κ_{eff}" data was slightly scaled; at the same

time, care was taken to ensure that the relative discrepancy between the "true CDF" and the "Reconstructed CDF, κ_{eff}" data in Fig. 12(b) is the same or smaller than that shown in Fig. 2 of Ref. [7].

[40] J.-P. M. Péraud, Ph.D. thesis, Massachusetts Institute of Technology, 2015.

[41] J.-P. M. Péraud and N. G. Hadjiconstantinou, Extending the range of validity of Fourier's law into the kinetic transport regime via asymptotic solution of the phonon Boltzmann transport equation, Phys. Rev. B **93**, 045424 (2016).

[42] K. Gordiz and A. Henry, Phonon transport at crystalline Si/Ge interfaces: The role of interfacial modes of vibration, Sci. Rep. **6**, 23139 (2016).

[43] I. S. Gradshteyn and I. M. Ryzhik, *Table of Integrals, Series, and Products*, 7th ed. (Academic Press, Burlington, Massachusetts, 2007).